RESEARCH ARTICLE

Synergistic effect between molybdenum back contact and CIGS absorber in the degradation of solar cells

Adèle Debono[1,2] | Hortense L'Hostis[1,2] | Amelle Rebai[2] | Erlind Mysliu[3] | Inger Odnevall[4] | Nathanaelle Schneider[2] | Jean-François Guillemoles[2] | Andreas Erbe[3] | Polina Volovitch[1,2]

[1]Chimie ParisTech-CNRS, Institut de Recherche de Chimie Paris (IRCP), PSL Research University, Paris, France

[2]Institut Photovoltaïque d'Île-de-France (IPVF), UMR 9006, CNRS, Ecole Polytechnique, IP Paris, Chimie ParisTech, PSL, Palaiseau, France

[3]Department of Materials Science and Engineering, Norwegian University of Science and Technology (NTNU), Trondheim, Norway

[4]KTH Royal Institute of Technology, Dep. Chemistry, Division of Surface and Corrosion Science, Stockholm, Sweden

Correspondence

Polina Volovitch, Chimie ParisTech-CNRS, Institut de Recherche de Chimie Paris (IRCP), PSL Research University, 11 rue Pierre et Marie Curie, 75005, Paris, France.
Email: polina.volovitch@chimieparistech.psl.eu

Abstract

The stability of molybdenum (Mo) back contact and $Cu(In_xGa_{(1-x)})Se_2$(CIGS) absorber layers interfaces relevant for CIGS-based solar cells was investigated using accelerated aging test, considering humidity and temperature daily variations as well as atmospheric pollution. Different configurations of sputtered Mo and co-evaporated CIGS layers deposited on soda lime glass with or without ALD-Al_2O_3 encapsulation were investigated. They were exposed for 14 days to 24 h-cycles of temperature and humidity (25°C at 85% RH and 80°C at 30% RH) with and without solution of the pollutant salts (NaCl, Na_2SO_4, and $(NH_4)_2SO_4$) deposited as drops on the sample to mimic marine, industrial, and rural atmospheric conditions, respectively. ALD-Al_2O_3 encapsulation failed to protect the samples against the pollutants regardless of configuration. The evolution of the films was characterized by Raman spectroscopy, grazing incidence X-ray diffraction, X-ray photoelectron spectroscopy, scanning electron microscopy, and energy-dispersive X-ray spectroscopy. Unencapsulated Mo degraded forming a mixture of oxides (MoO_2, MoO_3, and Mo_8O_{23}). Unencapsulated CIGS on glass substrates was not altered, whereas dark spots were visible at the surface of Mo/CIGS configurations. Further characterization evidenced that even though the Mo layer was buried, its corrosion products were formed on top of CIGS. Mo corrosion products and copper selenide, $Cu_{2-x}Se$, were identified in dark spots. Their formation and evolution were further investigated by in situ Raman spectroscopy. A speculative mechanism explaining the interplay of molybdenum and CIGS layers during aging is proposed. In place of Mo oxides, detected on the open surface of bare Mo, soluble molybdates are expected in confined environment where alkalinity locally increases. The molybdate ions may then react with sodium ions accumulated at the grain boundaries of CIGS, forming Na_2MoO_4. The latter could form $Na_2Mo_2O_7$ during drying because of pH decrease by atmospheric CO_2 adsorption. High pH in confined zone, combined with relatively high temperature, is also believed to lixiviate gallium into soluble tetragallates $[Ga(OH)_4]^{2-}$, which could precipitate into Ga_2O_3 with pH decrease leaving Ga depleted $Cu_{2-x}Se$.

1 | INTRODUCTION

Chalcopyrite Cu (In$_x$Ga$_{(1-x)}$)Se$_2$ (CIGS)-based photovoltaic cell comprises a widely used technology either as a single absorber CIGS cell (a world record of 23.6% efficiency has been reported by Evolar/Uppsala in 2023[1,2]) or as a subcell in tandem technologies.[3,4] Thanks to the high absorption coefficient (>10^5 cm^{-1}), it is possible to make CIGS photovoltaic cells thin enough to allow flexibility and reduce the use of raw materials.[5] As these cells are now produced on an industrial scale, long-term stability of such technology is important.

Under operating conditions, a photovoltaic (PV) system is facing multiple external stresses that can affect its performance: temperature, humidity, ultraviolet (UV), mechanical load (snow, wind), and so on. Reliability tests are designed for quality control of materials and devices in laboratory. These tests use the conditions which are suggested to be the most harmful and able to accelerate the aging. Among them, damp heat (DH) is the most common test examining temperature and humidity effects on aging. In DH, samples are aged for 1000 h at a constant temperature of 85°C and constant relative humidity (RH) of 85% (described in Standard EN 61215[6]). Temperature effects are also studied by thermal cycling: Temperature varies from −40 ± 2°C to 85 ± 2°C for 20 cycles with a maximum duration of 6 h/cycle (also described in Standard EN 61215, no specification for humidity[6]) in order to better mimic daily or seasonal temperature variations. To further replicate the outdoor conditions and in particular dew phenomena, we have recently proposed a novel degradation protocol.[7] It not only considers daily variations of temperature and humidity but also takes into account outdoor pollutants, well-known as corrosion promoters in corrosion science but rarely included in aging test in PV.[7–9]

To understand degradation processes, it is necessary to consider the complete cell architecture because the stability of each layer and interface can affect the stability of other layers and the overall cell performance. A typical architecture of a CIGS cell consists of several layers:

- substrate (glass for rigid or metal, polymer, or ceramic materials for flexible substrate);
- electrical back contact (usually molybdenum);
- p-type absorber (CIGS) covered by a thin n-type buffer (CdS or less toxic alternatives like Zn(O,S) and others);
- window layer (transparent conductive oxide like intrinsic zinc oxide and aluminum-doped zinc oxide [AZO]);
- top metallic grid contract (e.g., nickel/aluminum).[3]

On a module level, cells are encapsulated to limit the effects of the environment (water or oxygen ingress, UV radiation etc.). Glass is an excellent encapsulation material for rigid modules, but ultrathin glass, more adapted to flexible modules, is expensive and mechanically limited.[5] Multilayers of organic layers or stack of polymers and inorganic barriers, especially thin layer such as Al$_2$O$_3$, TiO$_2$, or SnO$_2$, are investigated as alternatives.[10] Recent work reported that CIGS cells with a 25-nm thick Al$_2$O$_3$ encapsulant can successfully pass 2000 h of the DH test.[11] Even if the mechanical protection could not be fully provided by this single layer, the present work is focused on the chemical stability so this encapsulation was selected for the study on the basis of its chemical stability in DH test.

According to the literature, the main cause of the efficiency loss of CIGS cells in the presence of humidity can be ascribed to the resistivity increase of the AZO layer.[12–14] Our previous work[7] has also demonstrated that the atmospheric aerosols can crucially decrease the life time of AZO. The combined effect of humidity and atmospheric aerosol pollution on other layers of the CIGS cell, in particular the back contact and absorber, was not reported in the literature to the extent of our knowledge.

Concerning the back contact, molybdenum (Mo) remains the material of choice because of its good conductivity, resistance to high temperatures[12] and limited diffusion in the CIGS layer.[15] However, it is very sensitive to humid environments, causing failure of the cell.[14] The scribes usually named P2 (interfacing the molybdenum and AZO layer) and P3 (interfacing the molybdenum with the atmosphere), necessary to create the series interconnected structures to reduce photocurrent and resistance losses, are especially sensitive to humidity.[15] The formation of molybdenum oxides (MoO$_x$ with 2 ≤ x ≤ 3) leads to a loss of conductivity, detrimental to the cell performance.[12,15] However, some other work suggests that MoO$_{3-x}$ could actually be beneficial for the cell as it is used to improve the carrier transport across the junction thanks to a large work function.[16] The formation of MoSe$_2$ at the interface between the molybdenum and CIGS improves the stability of molybdenum, particularly to oxidation.[9,15] Additionally, Na- and Se-containing products were observed on the surface of degraded molybdenum layer after DH tests.[15,17,18]

The CIGS absorber is not considered to be the most sensitive cell component to humidity in accelerated weathering tests. This layer contains some alkali elements (Na, K) at grain boundaries, which improve its electronic ability (increase in charge carrier concentration, passivation of defect at grain boundaries[19]) but can negatively influence stability against humidity.[20] Pure CIGS degradation is usually described in the literature by diffusion mechanisms of copper[21] or sodium[17,20,22] and oxidation.[21,23] The performance loss of the CIGS layer was described in the literature as occurring due to the formation of shunting paths (through which the electrons produced in the cell will preferentially recombine inside through the cell instead of being extracted at the top and bottom contacts) in the cell, created by

secondary phases of CIGS (e.g., $Cu_{2-x}Se$) or sodium compounds, which were indeed detected on the degraded surfaces.[22–25] Alkali elements (Na, K) are observed to be redistributed after aging.[20,26] The removal of corrosion products by mechanical scribing or chemical etching (e.g., using KCN) allowed the cell to recover its initial performance.[22,23] Since CIGS layer growth might be influenced by molybdenum morphology and composition, it can be expected that the Mo/CIGS interface is relevant in the long-term stability of PV cells.

The present work aims to improve the understanding of long-term outdoor stability of Mo/CIGS interface for flexible applications. Taking into account that thick glass encapsulation cannot be used in flexible structure, several secondary objectives are as follows:

i. To test the performance of the selected inorganic encapsulant (25 nm Al_2O_3) with respect to temperature/humidity and atmospheric pollutants for different systems.

ii. To verify the impact of the Mo/CIGS interface on the corrosion of the solar cell

iii. To understand the degradation mechanism of CIGS and molybdenum layers separately and in the Mo/CIGS stack on glass

To improve the understanding of CIGS degradation, stability of three different model configurations, molybdenum deposited on soda lime glass (SLG/Mo), CIGS deposited directly on glass (SLG/CIGS), and combined SLG/Mo/CIGS stack, with and without encapsulation was studied by a cyclic accelerating aging procedure[7] with temperature and humidity variations. Furthermore, the effect of atmospheric pollutants was tested by the deposition of three salts: NaCl, Na_2SO_4, and $(NH_4)_2SO_4$ typical of marine, industrial, and rural exploitation conditions, respectively. The proposed degradation mechanisms were supported by an in situ Raman spectroscopy during aging at controlled temperature and humidity.

2 | METHODOLOGY

2.1 | Materials and samples architecture

Prior to deposition, 3 mm thick soda lime glass substrates were washed by sonication in acetone, isopropanol (2 × 5 min), and dried with nitrogen blow. Molybdenum (Mo) was deposited on SLG by DC magnetron sputtering from a 99.95% pure Mo target as a bilayer, with a total thickness of 0.5 μm. A 1.5 μm thick CIGS layer was deposited by a three-step co-evaporation process as described elsewhere,[27] corresponding to copper-poor absorber composition (atomic ratios of CGI = Cu/(Ga+In) ∼ 0.80 and GGI = Ga/(Ga+In) ∼ 0.39, with the composition gradient from top to bottom, decreasing CGI, and increasing GGI). Such an absorber is characterized by a band gap of E_g ∼ 1.3 eV. CIGS layers were deposited either on SLG or on SLG/Mo substrates.

A 25 nm thick layer of Al_2O_3 was deposited by atomic layer deposition (ALD) from trimethylaluminum and H_2O at deposition temperature of 160°C, according to Zhang et al.[11] These process parameters were selected because it was reported that such a layer effectively protects AZO in DH for 2000 h.[11]

Five different configurations, referred as SLG/Mo/CIGS/Al_2O_3, SLG/Mo/Al_2O_3, SLG/Mo/CIGS, and SLG/Mo, SLG/CIGS (layers listed from bottom to top), were fabricated and tested in accelerated aging tests (see Table 1).

2.2 | Accelerated degradation protocols

The accelerated aging was performed in a climatic chamber "Weiss WKL 100" for a duration of 10 or 14 days (see Table 1). Temperature and RH were cycled over 24 h with targeted steps between 25°C at 85% RH and 80°C at 30% RH. This simulates day/night and seasonal variations as proposed in Zhang et al.[7] The recorded temperature and RH variations during one cycle are shown in Figure 1A. The arrow indicates the moment when the sample is under room conditions as it is taken out of the chamber for pollutant deposition and intermediate characterizations (visual observation, optical images, and Raman spectroscopy).

For each series, some samples were tested with salts typical of atmospheric aerosol pollutants. The corrosion process is very sensitive to water layer thickness on top of the material, and aqueous and atmospheric corrosion mechanisms can significantly differ. This is largely known for metallic corrosion of structural materials[28] and was also recently demonstrated for molybdenum in photovoltaic applications.[9] In function of conditions (temperature, humidity, atmospheric pollutants …), microdroplets are present in the atmosphere and could condensate on the surface. Cyclic drying and redeposition of new atmospheric aerosols could lead to the accumulation of salts on the surface up to several hundreds of mg m^{-2} day^{-1}.[28] To reach these concentrations, a 100 μL drop of an aqueous solution containing selected atmospheric pollutant (NaCl, Na_2SO_4, or $(NH_4)_2SO_4$) was deposited on the top of the sample daily for 5 days. The thickness and distribution of the electrolyte in the drop were naturally controlled by the humidity and temperature condition inside the climatic chamber. The concentrations of the solutions were as follows: 1.06 mmol. L^{-1} for NaCl, 0.78 mmol. L^{-1} for Na_2SO_4, and 0.78 mmol. L^{-1} for $(NH_4)_2SO_4$. These quantities were chosen to reproduce average salt

TABLE 1 Overview of samples per configuration and test duration.

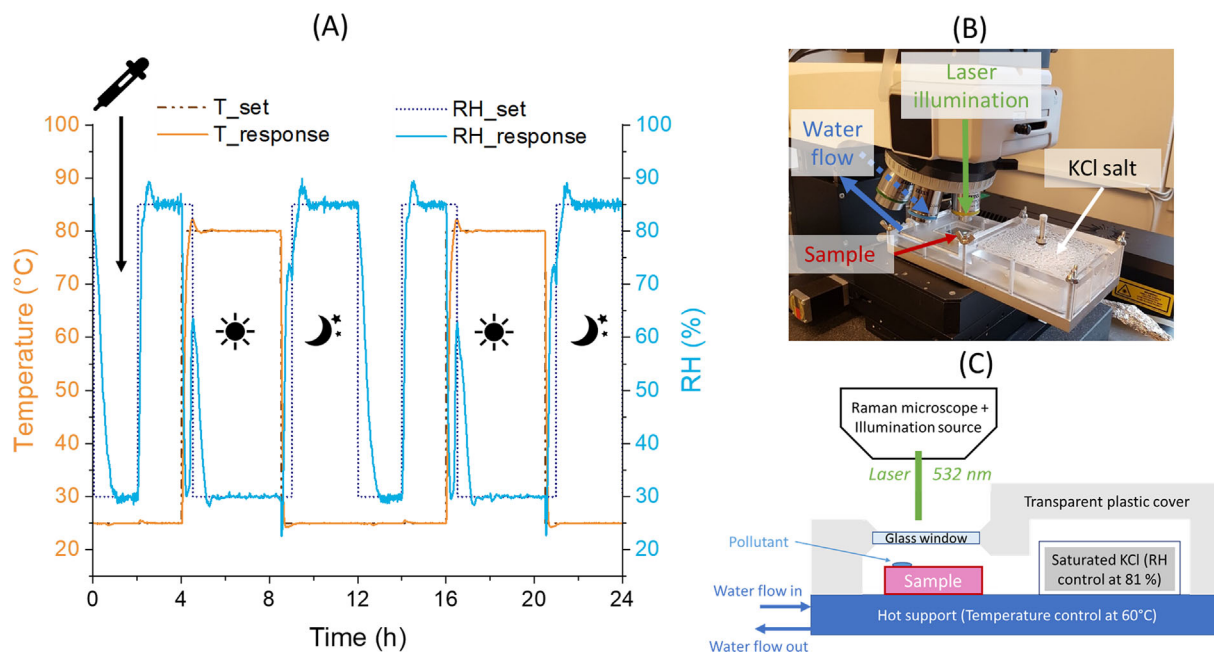| Configuration	Duration of test (days)
SLG/Mo/CIGS/Al_2O_3	14
SLG/Mo/Al_2O_3	14
SLG/Mo/CIGS	10 (4 samples)—14
SLG/Mo	14
SLG/CIGS	14

FIGURE 1 (A) Schematic representation of one cycle (24 h) of the accelerated aging test in climatic chamber: set (dotted lines) and actual (full lines) profiles of temperature (orange) and humidity (blue) in function of time. The arrow indicates the deposition of the salt solution. Cycle was repeated for several (10–14) days; (B) Photograph and (C) Schematics of the in situ Raman set up (temperature and humidity controlled, illuminated by 532 nm laser).

deposition of 7.5 $\mu g\,cm^{-2}\,day^{-1}$ of Cl^-, 15.0 $\mu g\,cm^{-2}\,day^{-1}$ of SO_4^{2-}, and 11.2 $\mu g\,cm^{-2}\,day^{-1}$ of NH_4^+ inside the drop. The daily deposition of NaCl and $(NH_4)_2SO_4$ was two times higher than in the previous work.[7] Na_2SO_4 was not previously tested therefore its concentration was calculated to ensure the same SO_4^{2-} deposition as from $(NH_4)_2SO_4$. The samples aged with pollutant salts are referred as "NaCl", "Na_2SO_4," and "$(NH_4)_2SO_4$." The samples that are referred as "No pollutant" were exposed to the same conditions in the climatic chamber but without drop deposition. Additionally, for each experiment and configuration, samples were kept in a desiccator under vacuum at room temperature and are referred to "Reference." To ensure the reproducibility of the results, at least two samples of each configuration were exposed to the same conditions ("No Pollutant", "NaCl", "Na_2SO_4," and "$(NH_4)_2SO_4$").

For the verification of the mechanistic hypotheses, additional experiments were made by in situ Raman measurements during 75 h of degradation of SLG/Mo/CIGS sample in a home-built Raman cell with temperature and humidity-control.[29] The setup is presented in Figure 1B. The temperature control was achieved through a hollow aluminum support with hot water circulating inside it (measured by the sensor, temperature inside the cell was 45°C). The humidity level was controlled by the presence of a saturated KCl solution in the connected compartment, leading to 80.4%–82.8% RH.[30] To accelerate degradation, the sample was illuminated by defocused green laser (532 nm at 30 mW) for a total of 54 h. The illuminated area was estimated with a diameter of 33 μm diameter from the back-reflection image; this gives an estimation of the average power density on the order of 10^7 W·m^{-2}. Please note that the

maximum temperature achieved in these conditions depends nontrivially on the spot size, incident power and substrate thermal conductivity. A study conducted in similar conditions leads to a maximal increase of temperature in the spot of 100 K.[31] The power has been chosen in a way that in a dry state under the beam there was no surface modification detected by either microscope or Raman spectra change. Three drops of 3 μL each, containing 7.81 mmol. L^{-1} $(NH_4)_2SO_4$ solution were deposited and dried before the aging in three selected area of the sample.

2.3 | Thin films characterization

Ex situ Raman spectroscopy was performed during the low temperature/low humidity stage of the climatic test (see previous section) and after the end of the aging. The Raman spectra and Raman mappings were made with a Renishaw InVia Raman spectrometer controlled by the software WiRE 4.2 with green laser ($\lambda = 532$ nm/2.33 eV – Nd-YAG double, maximum power 100 mW, spot size about 1 μm) at room temperature. The acquisitions lasted during 30 s to 2 min with accumulations of 15 or 30 s to avoid saturation of the detector. The choice of incident power and acquisition time depend on the material's light absorption, and it was each time carefully optimized to avoid degradation of the material while maximizing the signal/noise ratio. The acquisitions were made with 1800 lines/mm grating using a Leica DM2500 50× objective (NA 0.75). Cosmic ray removal followed by a noise reduction as well as empty modeling analysis for mapping were done using WiRE 4.2 software.

In situ Raman measurements were performed on a WITec 300R spectrometer with an objective Zeiss LD EC Epiplan-Neofluar Dic 50×/NA 0.55 and a green laser laser ($\lambda = 532$ nm – Nd-YAG double). The acquisition time was longer than for the ex situ Raman due to attenuation by the window of the cell and varies between 2 and 6 min with accumulations between 10 and 30 s. The laser spot size is expected to be close to the diffraction limit (1.2 μm of diameter) but certainly a little bigger due to the in situ cell's window. The operation and data analysis were performed by Project Five 5.2 software.

Scanning electron microscopy (SEM) images were taken with a Supra 35 (Zweiss) microscope at 15 kV at working distance of 15.0 mm and backscattered electron (BSE) images at 15 kV at working distance of 11.0 mm. Energy-dispersive X-Ray spectroscopy (EDS) was done with a Bruker XFlash 6|60 detector at 15 kV and working distance of 10.5 mm. Instrument control and data analysis were conducted by Quantax Esprit software.

Grazing incidence X-ray diffraction (GIXRD) patterns were collected using a PANalytical Empyrean diffractometer with a Cu Kα source ($\lambda = 0.154$ nm) in the 2θ range of 8°–75° with a step size of 0.2° at a scan speed of 0.04°/s and a grazing incidence angle at 0.3°. Bragg–Brentano XRD diffractograms were collected using a Cu Kα source ($\lambda = 0.154$ nm) on a PANalytical X'Pert Pro X-ray diffractometer in the 2θ range of 8°–75° with a step of 0.0263° at a scan speed of 0.058°/s.

The optical micrographs were taken with a VXH Keyence microscope with a VH-Z100R/W/T lens.

Elemental depth profiles were obtained by glow-discharge optical emission spectroscopy (GD-OES) with a G-Profiler 2™ (Horiba). The measurements were performed with a 4 mm anode and an Argon plasma at 450 Pa, power 20 W with asynchronous pulse at 3000 Hz.

Compositional analysis of the outermost surface oxide (information depth 5–10 nm) was performed using X-ray photoelectron spectroscopy (XPS, UltraDLD spectrometer, Kratos Analytical) using a monochromatic Al Kα X-ray source operating at 10 mA and 15 kV (150 W). All binding energies were calibrated versus adventitious carbon at 285.0 eV. Overview spectra and detailed high-resolution XPS spectra (20 eV pass energy) of C 1s, O 1s, N 1s, S 2p, Cl 2p, Mo 3d, Al 2p, Al 2s, and Si 2p were acquired for the SLG/Mo/Al$_2$O$_3$ configuration. The deconvolution of the N 1s peak considered the overlap with the Mo 3p peak. Due to peak overlap between Al 2p and Mo 4s, the Al 2s peak was used for the quantification.

For the SLG/Mo/CIGS/Al$_2$O$_3$ configuration, detailed spectra were acquired only for C 1s, Al 2p, Cu 3p, and In 4p. However, due to peak overlap between Cu 3p and Al 2p and between Cu 3s and Al 2s, the interpretations of any degradation of the Al$_2$O$_3$ layer on the CIGS surface are only speculative and not straightforward. Some assumptions were made based on atomic ratios of Cu 2p/In 3d determined from the SLG/Mo/CIGS reference and the results for the SLG/Mo/Al$_2$O$_3$ configuration area outside the (NH$_4$)$_2$SO$_4$ droplet.

3 | RESULTS

3.1 | Efficiency of Al$_2$O$_3$ encapsulation versus aerosol pollutants

The effectiveness of thin film encapsulation in service conditions was first checked in order to verify whether CIGS and molybdenum layers could be exposed to weathering. The observed tendencies are illustrated in Figure 2 on the example of SLG/Mo/CIGS/Al$_2$O$_3$ configuration. As can be seen in the figure, the surfaces of "Reference" and "No pollutant" samples appear homogenous at macroscopic level (upper images) and demonstrate typical grain structure of polycrystalline CIGS at higher magnification (lower images). When pollutants were present during exposure ("NaCl", "Na$_2$SO$_4$," or "(NH$_4$)$_2$SO$_4$)"), the surface outside the drop appears visually similar to the "No pollutant," while degradation is visible at macroscopic level inside of the area where the drop was deposited (upper images). Residues of deposited salts and corrosion products are present inside this area even after rinsing (down images).

Similar tendencies were observed for SLG/Mo/Al$_2$O$_3$ samples. XPS data (Table 2) show only a small dissolution of the Al$_2$O$_3$ layer outside the drop. Indeed, Al$_2$O$_3$ thickness seems to become less than 7–10 nm as some molybdenum signal is detected, but Al is still the major detected element (see the ratios of atomic concentrations of Al and Mo, expressed as Al/(Al+Mo) in Table 2). Still these results could suggest that cycling is probably more aggressive to Al$_2$O$_3$ than constant temperature and humidity solicitation, at least no decrease of thickness was reported in 1000 h of DH test in Zhang et al.[11] Al is, however, present only at the trace level inside the (NH$_4$)$_2$SO$_4$ drop, where mainly Mo is detected. The XPS results are therefore consistent with the visual observations and with literature[7] that while a 25 nm thick ALD-Al$_2$O$_3$ layer strongly limited the degradation of "No pollutant" samples (subjected only to the variations of temperature and humidity), it was inefficient in the presence of all the tested salts. The XPS results of this work are also consistent with the previous works, demonstrating that a 25 nm thick Al$_2$O$_3$ encapsulation on the AZO windows layers successfully passed the 1000 h DH test[11] but degraded in the presence of NaCl or (NH$_4$)$_2$SO$_4$ aerosols and temperature and humidity cycling.[7]

XPS also confirmed that Mo was mainly present as Mo (VI) oxides (Mo 3d$_{5/2}$ binding energies at 232.4 ± 0.1 eV and 233.3 ± 0.1 eV). Small Mo contribution was also observed at 228.3 ± 0.1 eV which could either be related to metallic Mo or it can also indicate the presence of Mo (IV) in MoO$_2$.[32]

The unexposed SLG/Mo/CIGS/Al$_2$O$_3$ configuration revealed the presence of the Al$_2$O$_3$ encapsulation layer without any detectable signal from the underlying CIGS layer. Due to peak overlap between Cu 2p and Al 2p as well as between Cu 2s and Al 2s, the Al-content could not be directly determined by XPS for the exposed SLG/Mo/CIGS/Al$_2$O$_3$ configuration. Based on the previous results, it can, however, be assumed that the Al$_2$O$_3$ layer remained largely unaffected outside the drop area upon exposure to (NH$_4$)$_2$SO$_4$ as observed for the
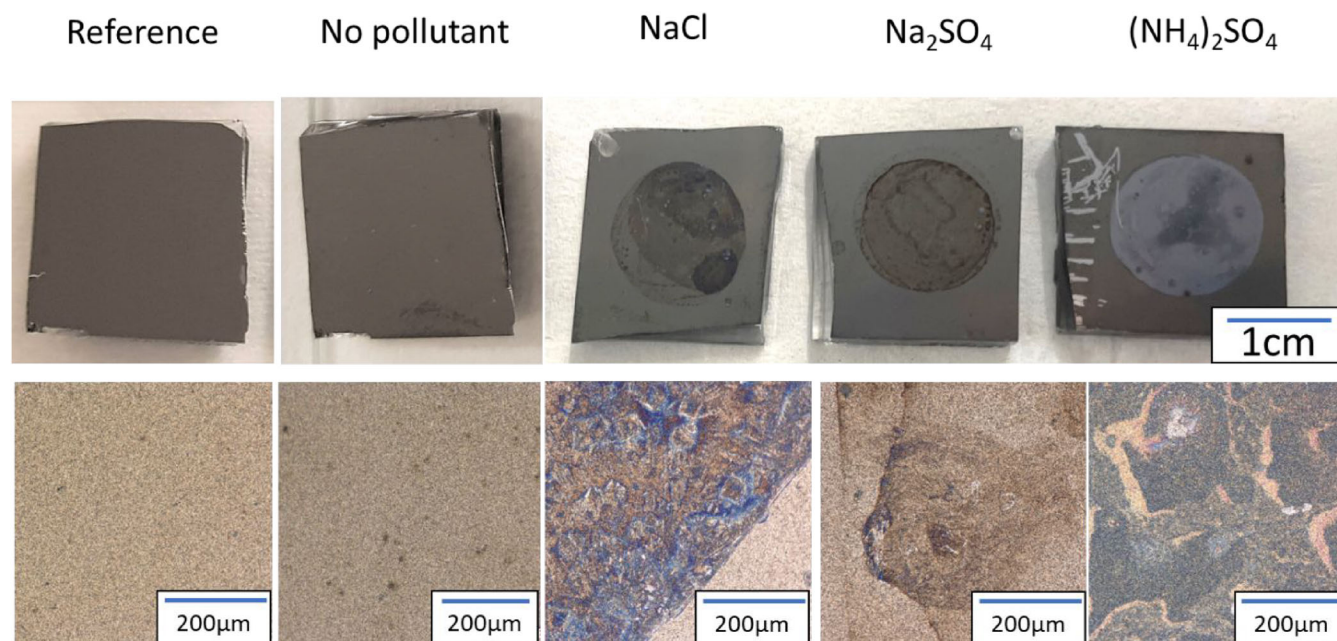
FIGURE 2 Typical visual aspect (top) and optical microscope images (bottom) of the unrinsed SLG/Mo/CIGS/Al_2O_3 samples (1.6 × 1.6 cm^2) after 14 days aging. Samples' names refer to the exposure conditions: in a desiccator ("Reference") or in a climatic chamber with ("NaCl", "Na_2SO_4", and "$(NH_4)_2SO_4$") or without ("No pollutant") pollutants. The white zones outside of the drop correspond to the scratches made after aging to marks some specific zones for further analysis.

TABLE 2 Atomic concentrations (at%) ratios for different elements (as indicated) on the top surfaces of samples before and after climatic tests and rinsing (from XPS).

Sample	SLG/Mo Reference	SLG/Mo/Al_2O_3			at.% measurement error
		Reference	$(NH_4)_2SO_4$ outside drop	$(NH_4)_2SO_4$ inside drop	
Al/(Al+Mo)	0	1	0.97	0.04	0.1

Sample	SLG/Mo/CIGS Reference	SLG/Mo/CIGS/Al_2O_3			at.% measurement error
		Reference	$(NH_4)_2SO_4$ outside drop	$(NH_4)_2SO_4$ inside drop	
Cu[a]/(Cu[a]+In)	0.30 ± 0.3	1	0.39 ± 0.3[a]	0.45 ± 0.5[a]	0.3–0.5

Abbreviation: XPS, X-ray photoelectron spectroscopy.
[a]The Cu 2p signal includes in the presence of Al_2O_3 also Al 2p signal—due to peak overlap can the amount of Al not be determined directly.

SLG/Mo/Al_2O_3 configuration. Indeed, if no Al_2O_3 remained, the Cu 2p/In 3d atomic ratio outside the droplet should be similar to unexposed configuration without Al_2O_3 (SLG/Mo/CIGS), here determined as 0.30 ± 0.3. However, since the calculated Cu 2p/In 3d atomic ratios were 0.39 ± 0.3, it means that the Cu content most probably was overestimated due to the presence and signal overlap with Al 2p. Inside the droplet, in contrast to the findings with SLG/Mo/Al_2O_3, Al was still present within SLG/Mo/CIGS/Al_2O_3 areas (Cu 2p/In 3d atomic ratios ∼ 0.45 ± 0.5). This indicates that the dissolved Al probably forms other reaction products with, for example, S and the CIGS metals within the droplet area.

These results do not exclude the possibility for a better encapsulation with ALD-Al_2O_3 with a different preparation (like with a thicker layer), but the test of the effect of the encapsulation thickness is out of the scope of this publication. The next sections therefore report the results on the degradation of unencapsulated samples in order to understand the degradation mechanisms related to Mo/CIGS interface.

3.2 | Effect of molybdenum back contact on the stability of SLG/CIGS and SLG/Mo/CIGS

In the absence of pollutants, visual observations and optical microscopy illustrated in Figure 3 show clear difference in the surface morphology of degraded samples between configurations with and without molybdenum (SLG/CIGS vs. SLG/Mo/CIGS), suggesting some differences in degradation mechanisms. Indeed, while no degradation
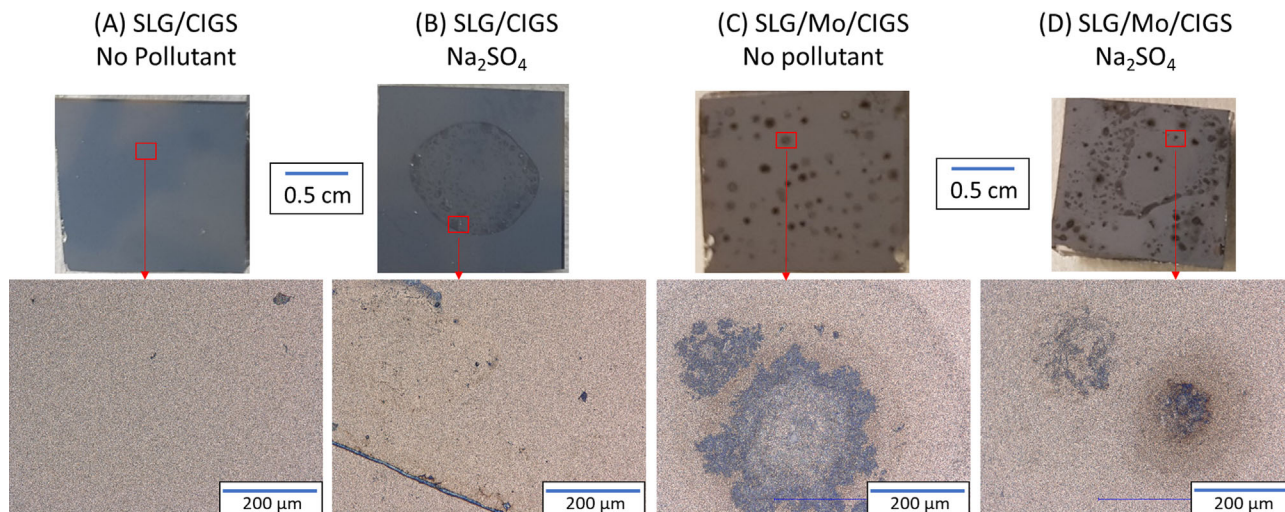
FIGURE 3 Typical visual aspect of 14 days aged SLG/CIGS and SLG/Mo/CIGS samples before rinsing (top) and high magnification optical micrographs of the same samples after rinsing (bottom). Samples exposed without salt pollutant and with a drop containing Na_2SO_4 are compared.

is visible on SLG/CIGS samples after 14 days in the climatic chamber (Figure 3, SLG/CIGS "No pollutant"), large (up to 600 μm) dark spots appeared on SLG/Mo/CIGS samples (Figure 3, SLG/Mo/CIGS "No pollutant"). There were about 24 spots/cm^2 (30, 80, and 72 points on 1.6×1.6 cm^2). Similar spots were observed after 5 h of DH test for SLG/Mo/CIGS[24] and after 50 h of DH test for Stainless Steel/Mo/CIGS/CdS[25] and were assigned to locations enriched in sodium. However, literature does not give a detailed explanation of how the spots are formed not of the presence of sodium inside them. Probably other alkaline cations could have similar effect; however, this hypothesis needs verification. The spots could not be removed by rinsing the surface. This indicates that degradation results in formation of insoluble products or modification of the CIGS composition and structure inside the spots and not only in formation of soluble corrosion products.

Dark spots were visible on the surface of SLG/Mo/CIGS samples aged with or without pollutants. For the samples tested with pollutants solutions, the deposit from the pollutant solution salts crystalized on the surface, leaving a visible trace of the drop. When rinsed, the salts crystals were mainly removed, indicating that the majority of the deposit is soluble. However, visual modifications remained at the edge of the drop for SLG/CIGS. This suggests that the effect of the pollutants in humid condition is not limited to the deposition of soluble salts but also modifies degradation mechanisms leading either to the formation of new corrosion products or to the irreversible degradation of the CIGS layer.

These observations point out the importance of Mo/CIGS interface in the degradation mechanisms of CIGS cells exposed to humid atmospheres. To understand the interplay between the layers during corrosion and elucidate degradation mechanisms, chemical changes occurring after degradation of SLG/Mo, SLG/CIGS and SLG/Mo/CIGS were studied separately and compared.

3.3 | Chemical evolution of molybdenum in SLG/Mo and SLG/Mo/Al$_2$O$_3$ configurations

Raman spectra were acquired every day of the cyclic test, under ambient conditions to evaluate the chemical evolution of the samples. The development of molybdenum corrosion products could differ between SLG/Mo and SLG/Mo/Al$_2$O$_3$ configurations because of the presence of confined zone in the latter. The "Reference" samples did not show any specific Raman peak (Figure 4—reference spectrum and Figure 5, spectra 1 and 3) which is coherent with the metallic surface.[15] The spectra shown in Figure 4 were acquired with a laser power of 10 mW. The laser power was carefully chosen to avoid the chemical transformation of the surface by laser illumination because at the laser power threshold between 10 and 50 mW (with an estimated laser spot area of 4 μm^2), the corrosion products of Mo irreversibly transformed into Mo_4O_{11}.

After 4 days of aging in the climatic chamber without pollutant, no visible modification occurred on SLG/Mo/Al$_2$O$_3$, but an orange color was observed on the surface of SLG/Mo (Figure 4, zone 1), substituting or covering the mirror-like metallic molybdenum. The Raman peaks at 956 cm^{-1} is attributed to be the $Mo^{6+} = O$ stretching mode of terminal oxygen atoms described in literature as being created by the breaking of Mo_2–O bonds at the corner-shared oxygens, possibly due to monoclinic m-Mo_8O_{23}.[33,34]

After 14 days, the surface was covered by isolated blue oxide islands surrounded by yellow oxide (Figure 4, zone 2) and some blue and rainbow iridescent areas (Figure 4, zone 3). The interference fringes may be due to a change in thickness of the molybdenum oxide layer. In both areas, a mixture of molybdenum oxides was present: monoclinic m-$Mo^{+IV}O_2$, orthorhombic α-$Mo^{+VI}O_3$, and monoclinic m-Mo_8O_{23} and MoO_{3-x}. The next paragraph details how the species were identified.
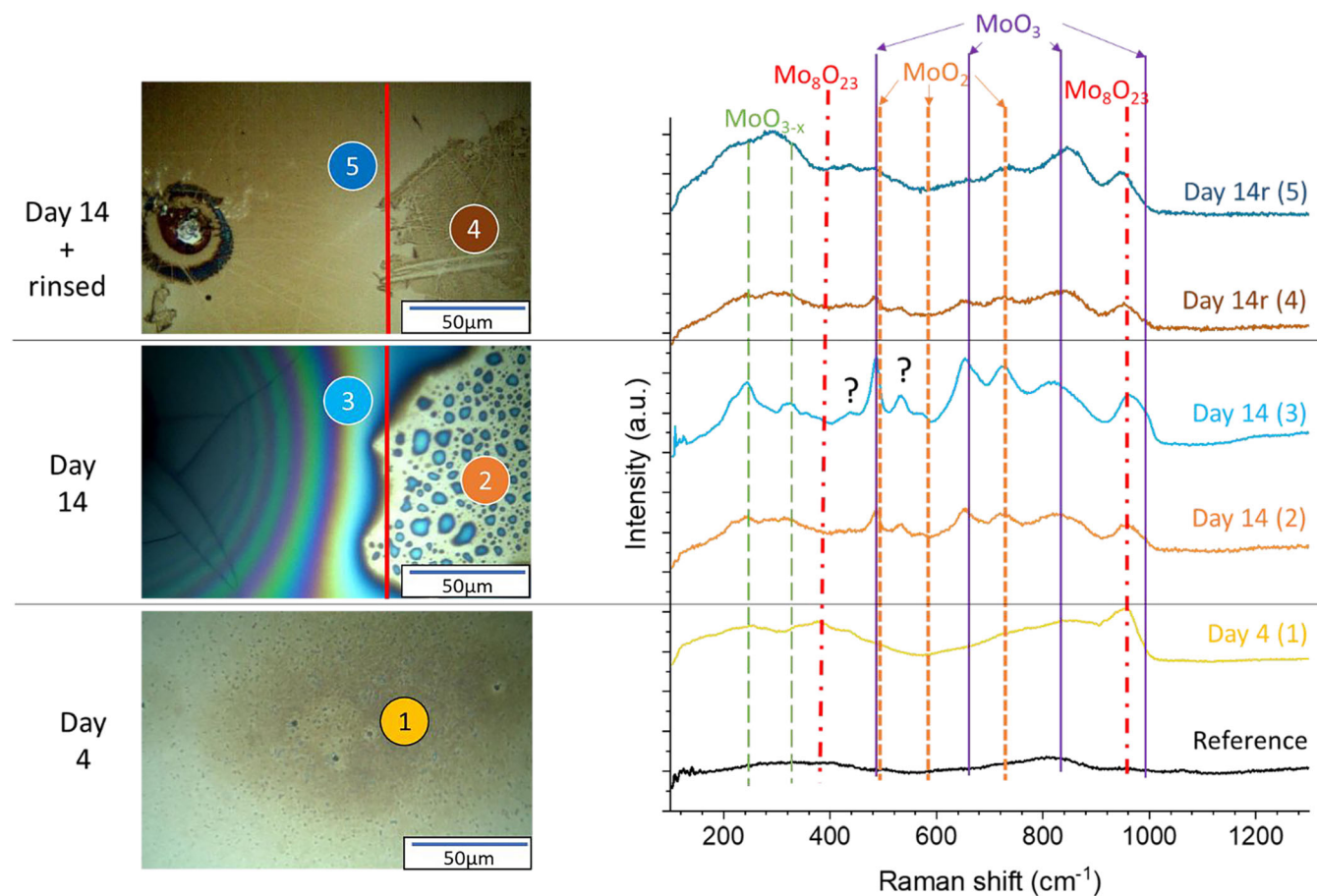
FIGURE 4 SLG/Mo "No pollutant": optical microscope images with Raman spectra associated to SLG/Mo evolution degradation in climatic chamber without pollutants at Days 4 and 14 and Day 14 after rinsing (Day 14r), normalized on value at 1200 cm^{-1}. Labels on the left indicate position of the recorded spectra on the right.

The Raman peaks around 485, 570, and 720 cm^{-1} were attributed to m-MoO$_2$[35] and peaks around 245, 320, and 377 cm^{-1} to MoO$_{3-x}$ molybdenum oxides and suboxides with $0 \leq x \leq 1$.[35] The peaks at 485, 650, 820, and 996 cm^{-1} are attributed to α-MoO$_3$ corresponding to B$_{1g}$-v (OMo$_3$), B$_{3g}$-v (OMo$_3$), B$_{1g}$-v (OMo$_2$), and A$_g$, B$_{1g}$-v$_{as}$ (Mo = O) modes, respectively.[35,36] The peak at 960 cm^{-1} is possibly due to m-Mo$_8$O$_{23}$.[33] The absence of Mo$_4$O$_{11}$ main peak at about 910 cm^{-1} [37] and of Mo$_{18}$O$_{52}$ main peak at about 1014 cm^{-1} [38] exclude them from the possibilities. The proposed identification of each peak is detailed in the supporting information Table S1. Similar Raman spectra were reported in other studies[15]: for SLG/Mo after 670 h at 60°C/60% and List et al.[39] for boro-aluminosilicate Glass/Mo after 168 h at 84°C/85% but without detailed identification of the oxides.

After rinsing, the apparent color of the right zone changed from blue/yellow to dark brown. In this zone, Raman spectrum remained unchanged (spectrum 2 vs. spectrum 4 in Figure 4), indicating that the oxides present in this zone were adherent and not entirely soluble. In contrast, in the left zone, the initially blue section turned to light brown and the spectrum after rinsing differed from the spectrum before rinsing (spectrum 3 vs. spectrum 5 in Figure 4). Some

peaks of Mo$_8$O$_{23}$ (peak at 950 cm^{-1}) and MoO$_2$ (peaks at 479 and 738 cm^{-1}) are still present, but the intensity of peaks from MoO$_3$ decreased significantly (peaks at 495 and 650 cm^{-1}). There is therefore either dissolution or adhesion loss of some oxides during rinsing. There was no recovery of the initial aspect of the surface nor spectrum after rinsing; thus, the material was irreversibly altered. Both factors, namely, the loss of metallic layer by corrosion with formation of soluble products and the accumulation of insoluble resistive products, can be detrimental for the solar cell performance as it leads to resistive losses.

On the samples aged with pollutants, new Raman peaks appeared on both encapsulated and unencapsulated samples. This is illustrated in Figure 5 for the example of Na$_2$SO$_4$ pollutant. Some peaks are due to the presence of sulfate salt (indicated by * in the figure), with specific Raman bands at 457 or 463 cm^{-1} that can be assigned to v$_2$(E), 619 and 635 cm^{-1} to v$_4$(F$_2$), main peak at 995 cm^{-1} to the main vibration mode v$_1$(A$_1$), and peaks at 1079, 1129, 1198 (spectrum 4), or 1125, 1193 (spectrum 2) cm^{-1} to v$_3$(F$_2$).[40] Compared with the vibration spectrum of Na$_2$SO$_4$, solid, hydrated, or in aqueous solution (see Table S2 in the supporting information), a slight shift and the absence of some peaks suggest that the sulfate reacted with the surface and
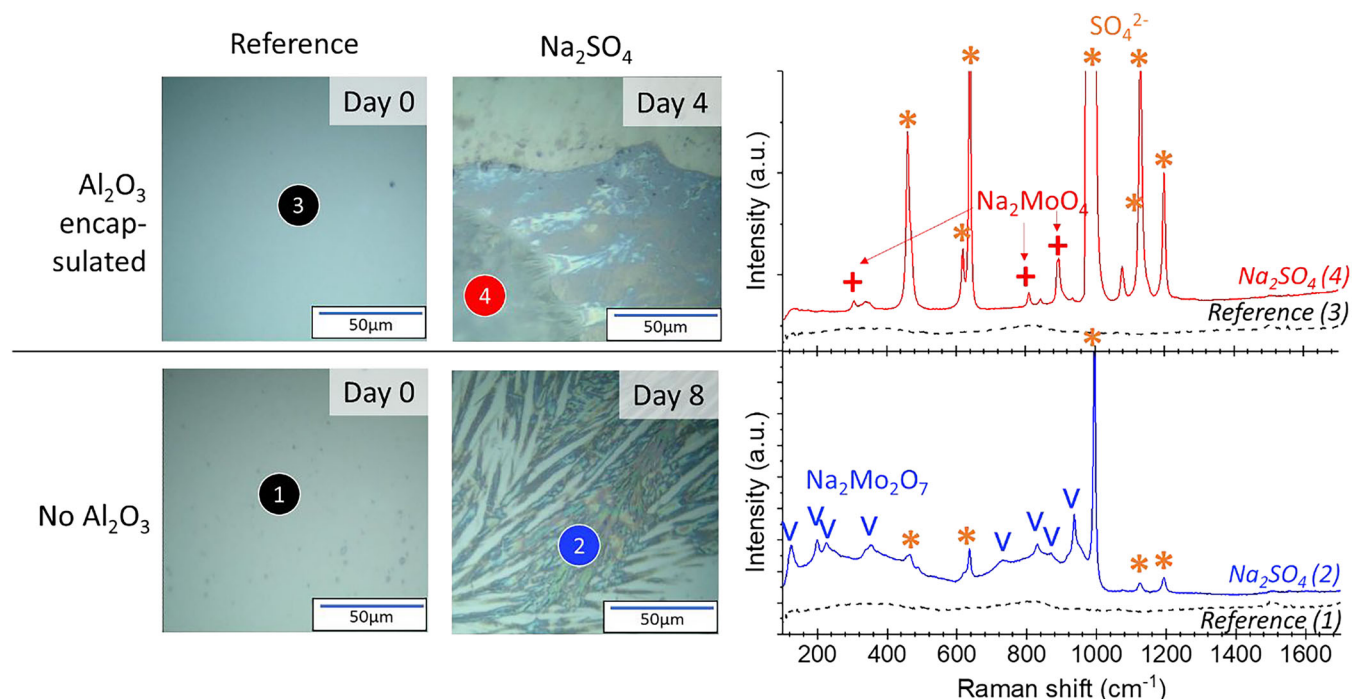
FIGURE 5 Example of optical microscope images and normalized Raman spectra of indicated zones on SLG/Mo and SLG/Mo/Al$_2$O$_3$ before ("Reference" in dash line) and after 4 or 8 days of aging with "Na$_2$SO$_4$" pollutant. The spectra were acquired for 4 × 15 s with a laser power of 10 mW for nos 1, 2, and 3 and 50 mW for no. 4.

the latter contains another sulfate. Another possibility is that water is incorporated into the sulfate. However, the shift of peaks position to higher Raman shift is not consistent with the global downshift when hydrated observed by Ben Mabrouk et al.,[40] that they attributed to the increase of interatomic distances because to the presence of OH groups.

More interestingly, new molybdenum containing species were detected in these conditions. For the encapsulated sample in spectrum 4 of Figure 5, the peaks at 307, 809, and 895 cm^{-1} were identified as belonging to MoO$_4^{2-}$ species. The absence of 852 cm^{-1} peak of K$_2$MoO$_4$[41] makes Na$_2$MoO$_4$ a more probable candidate.[42] This species was previously observed on the surface of degraded molybdenum in several studies: on SLG/Mo after 1000 h at 85°C/85%,[18] on SLG/Mo in deionized water for 24 h at 50°C,[17] and described as a possibility in Lin et al.[19] In our study, it was only detected on the surface of the encapsulated configuration (SLG/Mo/Al$_2$O$_3$) between 4 and 10 days of degradation but was not found after 14 days of the exposure.

The peaks at 124, 199, 226, 353, 729, 830, 871, and 937 cm^{-1} were detected on the surface of nonencapsulated SLG/Mo samples (spectrum 2 of Figure 5). These peaks perfectly fit with the positions expected for disodium dimolybdate Na$_2$Mo$_2$O$_7$.[43] This polymolybdate compound has not been previously reported for SLG/Mo systems degraded under DH conditions. It consists of infinite chains of MoO$_4$ tetrahedral bridges and adjacent MoO$_6$ octahedra.[43] This species was also only detected during the intermediate stages but not at the end of the cycling procedure.

More details about Raman peak identification of Figure 5 can be found in the supporting information Table S3. The Raman technique allowed the identification of chemical form, that is, precipitated or condensed molybdate salts and excluded the hypothesis of Na$^+$ intercalated in MoO$_x$, which was previously proposed to explain the presence of Na on the top surface of degraded Mo.[18]

Overall, the humidity-temperature degradation of SLG/Mo leads to the formation of a mixture of molybdenum oxides and suboxides as the major corrosion product in conditions without pollutants. In the presence of Na$_2$SO$_4$, sulfate ions are detected, along with Na$_2$MoO$_4$ and Na$_2$Mo$_2$O$_7$ that are formed on the encapsulated and nonencapsulated samples, respectively.

3.4 | Chemical evolution of SLG/CIGS and SLG/Mo CIGS in climatic test

As presented in Section 3.2 (Figure 3), SLG/CIGS without pollutant showed no visible degradation. The "Reference" and "No pollutant" samples were inspected with Raman, XRD (Figure S1 in the supporting information) and GIXRD (Figure S2 in the supporting information). The 2θ peaks in XRD and GIXRD patterns were attributed to CIGS: 27.1°, 36.1°, 45.3°, 53.3°, 65.5°, and 72.1° belong to (112), (211), (204)/(220), (116)/(312), (400), and (316) orientations, respectively (JCPSD 01-083-3360). From Raman, XRD and GIXRD, no chemical changes were observed for SLG/CIGS without pollutants, and only sulfates due to salt deposition were detected on the samples tested

with pollutants. The degradation SLG/CIGS without the molybdenum layer was thus below the sensitivity of the methods used. Therefore, this configuration is far less sensitive to temperature and humidity than SLG/Mo/CIGS.

Unlike the SLG/CIGS configuration, all samples of SLG/Mo/CIGS after aging showed visible degradation with the appearance of dark spots on the surface (Figure 3). The GIXRD (Figure S2) pattern of "Reference" of the SLG/Mo/CIGS shows 2θ peaks attributed to CIGS (JCPSD 01-083-3360, same as SLG/CIGS) and as well as 40.5° corresponding to the (110) orientation of molybdenum (JCPSD 04-014-7435).

A small peak at 8.5° appeared in the GIXRD spectra after aging with and without the pollutants, compared with the "Reference." The compound responsible for this peak is concentrated on the surface because its signal was more intense using GIXRD than XRD. The 8.5° peak disappeared after rinsing so it is suspected to be a soluble corrosion product or a precipitate with low adhesion at the surface. We attribute this peak to the presence of polymolybdates on the SLG/Mo/CIGS sample, as, for example, the (200) diffraction peak of $Mo_{17}O_{47}$ (JCPSD 00-013-0345)[44] or the (011) diffraction from $Na_2Mo_3O_{10}(H_2O)_3$ (JCPSD 01-087-1785).

The Raman spectrum (laser power 10 mW) of the "Reference" SLG/Mo/CIGS sample, used as reference in Figures 6-8, coincides with CIGS reference spectra. The main peak at 175 cm^{-1} was identified as A_1 vibration mode of Cu (In,Ga)Se$_2$,[45] the minor peak at 215 cm^{-1} to B_2/E stretching vibrational mode of CIGS,[46–48] and the second minor peak at 120 cm^{-1} to B_1 mode of CuInSe$_2$.[49] The EDS spectrum of the same sample confirmed the presence of Cu (L_α at 0.94 eV), Ga (L_α at 1.10 eV), In ($L_{\alpha 1}$ at 3.29 eV, $L_{\beta 1}$ at 3.50 eV, $L_{\beta 2}$ at 3.72 eV, and $L_{\gamma 1}$ at 3.94 eV), and Se (L_α at 1.39 eV).

The Raman signals detected on the aged CIGS ("No pollutant") sample in the zones outside the dark spots were similar to the "Reference" (not illustrated here), indicating that chemical changes were limited to dark spots.

Inside the dark spots, however, several changes in Raman spectra were observed, as illustrated by Figures 6-8. A peak at 259 cm^{-1} (spectrum 1 in Figure 6) can be attributed to the A_1 mode of Cu–Se compound (Cu$_{2-x}$Se).[45] This compound was proposed in the literature to be detrimental for the solar cell performance because it creates shunt paths. It is usually removed from CIGS surface by KCN etching but is known to appear again after deterioration of the PV cell.[22]

Formation of new corrosion products inside dark spots on the SLG/Mo/CIGS is illustrated in Figure 7 by the spectrum of point 2 (recorded with laser power 5 mW). The peaks at 114, 175, 223, and 256 cm^{-1} can be attributed to CIGS[45] and Cu$_{2-x}$Se, while the bands 305, 380, 808, 840, and 889 cm^{-1} correspond to the same molybdate as in Figure 5, spectrum 4. EDS spectra (not shown here) exhibiting signal from Mo, Na, and O in point 2 and none from K. Both Raman and EDS lead to the identification of this species as sodium molybdate Na$_2$MoO$_4$.[42] Outside the spots, the EDS and Raman spectra were similar to the "Reference" (neither Mo, Na, and O in EDS nor Na$_2$MoO$_4$ Raman peaks), confirming that sodium molybdate on the SLG/Mo/CIGS surface appears only in localized dark spots.

In some dark spots formed on the samples after 2 days aging (point 3 in Figure 8), the EDS confirms the presence of Mo ($L_{\alpha 1}$ at 2.29 eV and $L_{\beta 1}$ at 2.40 eV), Na (K_α at 1.04 eV), and O (K_α at 0.52 eV). For such locations, as illustrated in Figure 8, the Raman spectrum evidences the presence of molybdate, identified as disodium dimolybdate Na$_2$Mo$_2$O$_7$ by the peaks at 125, 339, 370, 528, 829, 870, 916, and 938 cm^{-1}[43] together with CIGS (175 and 229 cm^{-1} peaks) (Raman spectrum (3) in Figure 8, taken with laser power 5 mW). The atomic ratios of the elements obtained from the EDS spectra, shown in the right side of the Figure, were At. %(Mo)/At. %(Na) = 0.9 and At.%(O)/At.%(Na) = 3.2. These values are very close to the ratios expected for
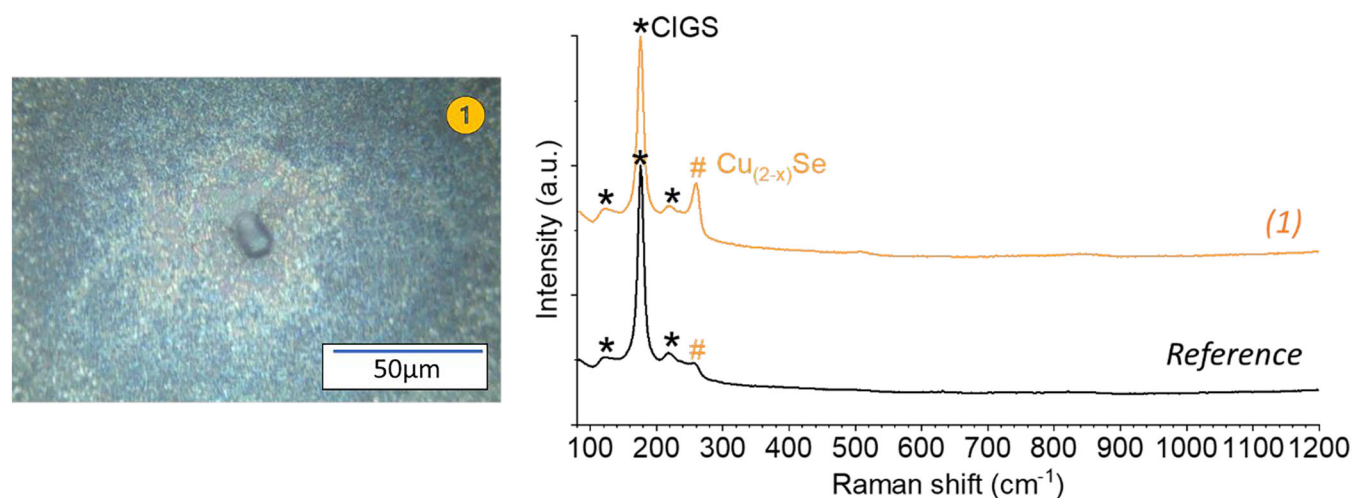

FIGURE 6 Example of Raman spectrum with associated optical image of point "1" localized inside the dark spots on the SLG/Mo/CIGS sample aged at temperature and humidity cycling without pollutants for 2 days compared with the initial "Reference" spectra measured before aging.
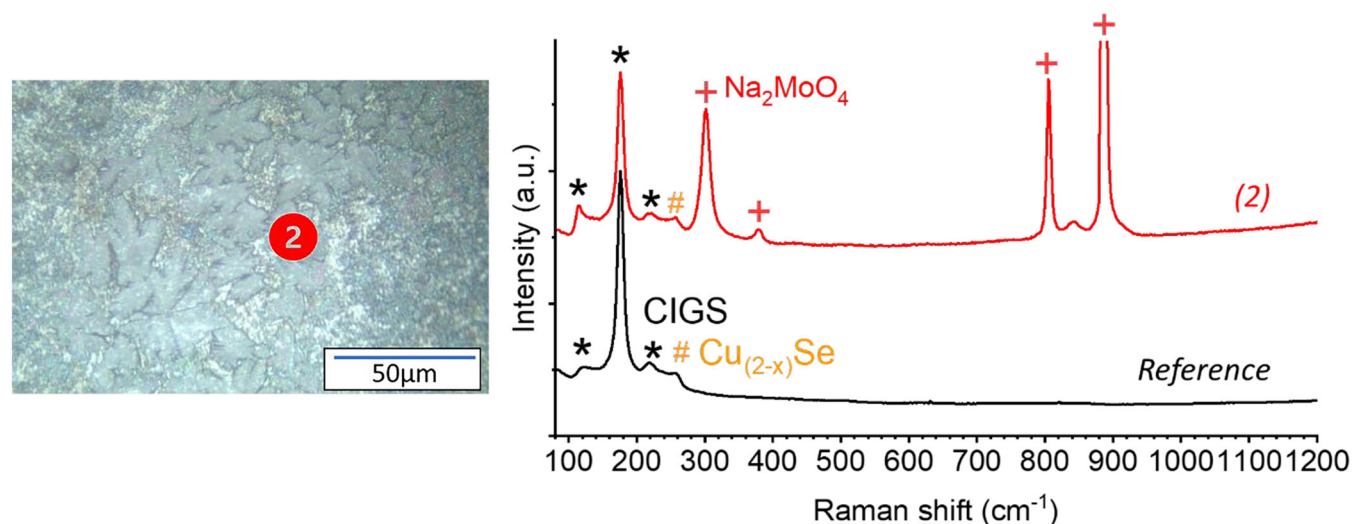
FIGURE 7 Raman spectrum with associated optical image of point "2" for SLG/Mo/CIGS No pollutant after 4 days aging compared with the initial "Reference" spectra measured before aging.
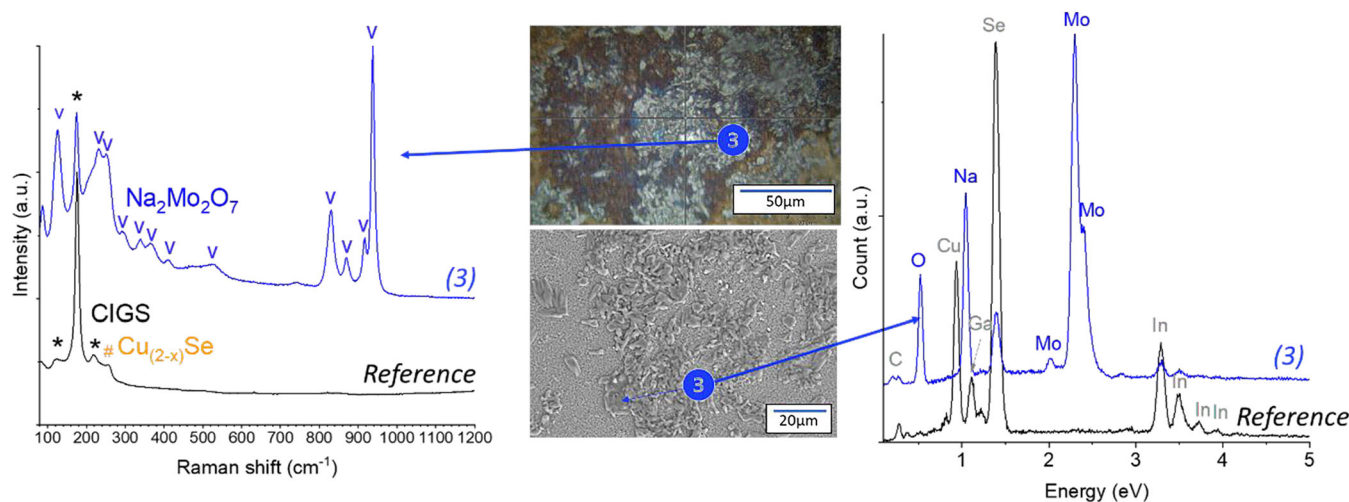

FIGURE 8 Raman spectrum (left) with associated optical image and energy-dispersive X-ray spectroscopy (EDS) spectrum (right) with scanning electron microscopy (SEM) associated image of point "3" for SLG/Mo/CIGS "No pollutant" aged for 2 days compared with the initial "Reference" spectra measured before aging.

$Na_2Mo_2O_7$: At.%(Mo)/At.%(Na) = 1 and At.%(O)/At.%(Na) = 3.5, corroborating the identification of the Raman spectrum.

Interestingly, the Raman spectra of the samples evolved also after a long period of storage under vacuum in desiccators: less Na_2MoO_4 and more $Na_2Mo_2O_7$ was detected inside the spots. This suggests that Na_2MoO_4 tends to polymerize into polymolybdate $Na_2Mo_2O_7$. The peak identification for Figures 6–8 is detailed in the supporting information Table S4.

In summary, localized degradation of SLG/Mo/CIGS samples during cyclic temperature and humidity variations resulted in formation of dark spots in which two sodium molybdates were detected at different times of aging. These molybdates were detected on the surface of the sample despite the fact that the molybdenum layer was buried

under the CIGS layer and no molybdenum was initially present on the surface. Localized enrichment of CIGS by a binary copper selenide $Cu_{2-x}Se$ was also detected in the dark areas.

3.5 | In situ study of SLG/Mo/CIGS degradation at constant temperature/RH condition

To understand degradation mechanisms and verify that the presence of molybdenum corrosion products on the top surface of CIGS is not related to a pre-existing local defect, aging experiments were carried out in a specifically designed in situ Raman cell allowing to control humidity and temperature (see Section 2.2, accelerated degradation
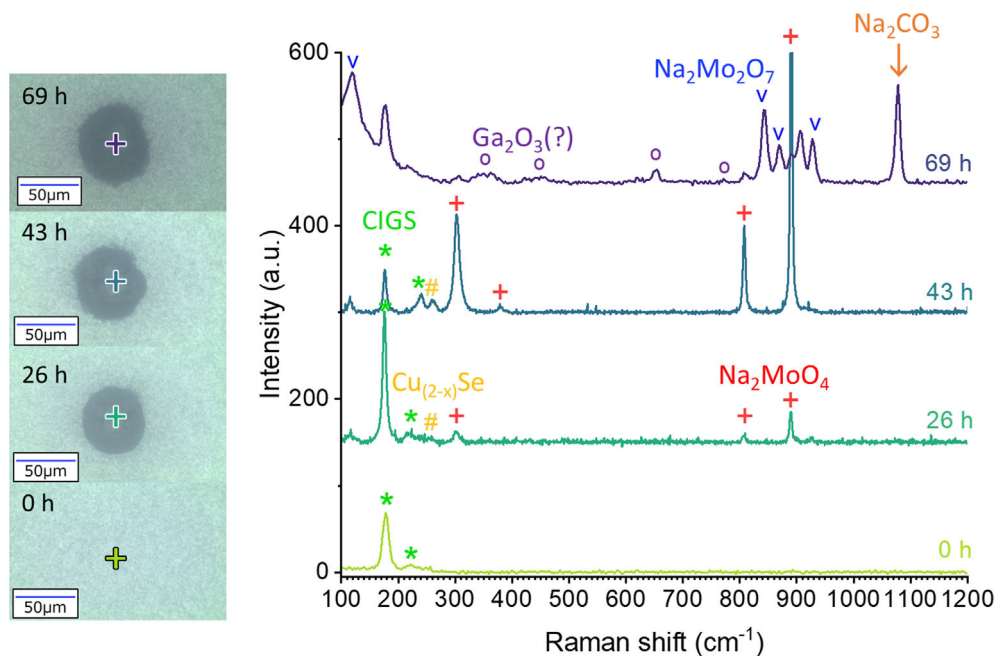
FIGURE 9 Evolution optical images and corresponding Raman spectra during formation of a dark spot on the surface of SLG/Mo/CIGS sample aged in the in situ cell (45°C, 82% RH, defocused laser illumination, three drops with $(NH_4)_2SO_4$).

protocols) under continuous defocused laser illumination. The continuous illumination and the confined environment of the thin layer cell were expected to accelerate degradation.

Dark spots appeared during aging in the in situ Raman cell after less than 2 days exposure. After 4 days of exposure, there were approximately 13 spots/cm^2 (49 spots/3.8 cm^2). Such concentration of spots was comparable with what was seen in the climatic chamber experiment; however, in contrast to the variety of ex situ spots sizes and shapes, all the in situ spots had very similar round shape with a 50 to 100 μm of diameter.

The time evolution of one spot in the in situ experiment with corresponding Raman spectra inside the spot is illustrated in Figure 9 (5 mW laser power, grating 600 g/mm for 0 and 69 h, and 1800 g/mm for 26 and 43 h). Initially, the surface looks homogeneous, with a Raman peak at 175 cm^{-1} attributed to CIGS. After less than 26 h, dark spots appeared. Raman peaks at 303, 380, 809, and 891 cm^{-1} inside the spots indicate the presence of Na_2MoO_4 on the surface. The intensity of Na_2MoO_4 peaks increases with time, while CIGS decreases between 26 and 43 h. The signal at 259 cm^{-1} ($Cu_{2-x}Se$) also increases between 26 and 43 h. After 69 h, the signal of Na_2MoO_4 decreases to the expense of others. New peaks fit well with a mixture of several species: Na_2CO_3, $Na_2Mo_2O_7$, $(NH_4)_2Mo_2O_7$, and Ga_2O_3. The identification is described in the next paragraph.

The new peaks at 69 h are visible at 120, 650, 843, 871, 907, 927, and 1077 cm^{-1}. The latter peak at 1077 cm^{-1} corresponds well with the main stretching mode ν_1 (A'_1) of a carbonate anion. The exact nature of the carbonate is not sure as a small shift may happen in a humid environment as compared with the spectrum of the solid species. The most likely species is Na_2CO_3 (main peak position between 1069 and 1080 cm^{-1}[150]) or $(NH_4)_2CO_3$ (main peak position at 1074 cm^{-1}[151]). K_2CO_3 is, however, less probable as its ν_1 (A'_1) mode is described to be below 1068 cm^{-1} even in aqueous

form.[50,52] The remaining peaks could be attributed to a mixture of polymolybdates $Na_2Mo_2O_7$ (peaks at 120, 843, 871 cm^{-1}, and possibly 927 cm^{-1}[143]) and $(NH_4)_2Mo_2O_7$ (843, 907, and 927 cm^{-1} peaks[53]). The peaks at 350, 450, and 650 cm^{-1} are suggested to be related to Ga_2O_3.[54]

The degradation conditions during aging in the climatic chamber and in the in situ Raman experiment are different, which can result in differences in the degradation rates and potentially some mechanistic steps. Therefore, it requires cautious interpretation. For example, the presence of carbonate can be due to the accumulation of CO_2 from air, which could be expected if the surface pH is increased rapidly in confined zone created by condensation. The fact that this carbonate appears together with polymolybdate anion is coherent with molybdate anion polymerization at high pH, expected from the revised Pourbaix diagram of Mo.[55] Comparing the evolution of different species, some interesting features to be noted:

i. The formation of sodium molybdate correlates with the presence of copper selenide in both conditions.
ii. Sodium molybdate with aging transforms into polymolybdate species.

Additionally, comparing the evolution of the in situ spectra taken in different locations of the dark spot during its expansion suggested that first $Cu_{2-x}Se$ expands from the center to the periphery and then molybdates appear in these zones. Although such an in situ observation needs to be confirmed with more data and statistical verification, it seems to be coherent with the distribution of corrosion products after the end of the experiment, as illustrated in Figure 10 by the results of confocal Raman mapping.

More information about the spatial distribution of the species inside the dark spot can be seen from the additional ex situ Raman
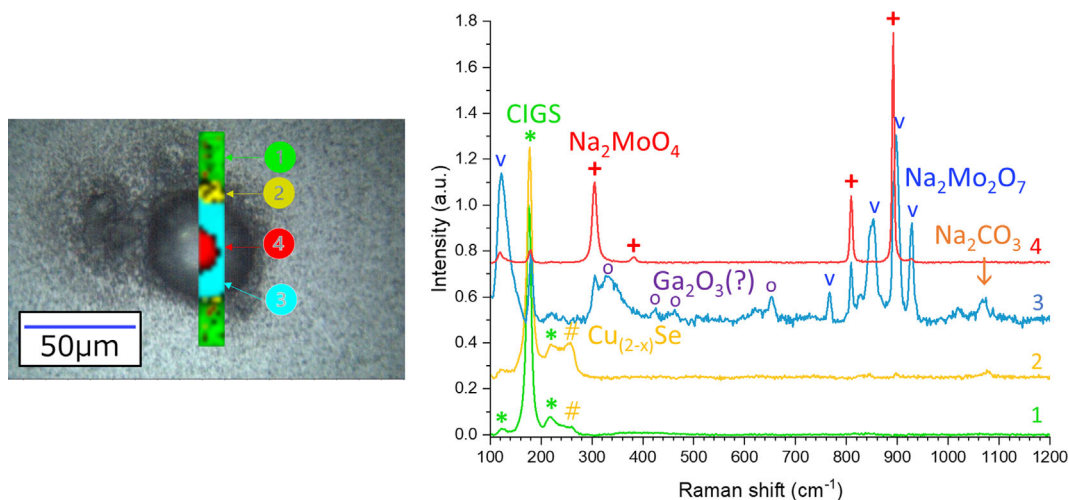
FIGURE 10 Raman map (recorded ex situ) of the dark spot on SLG/Mo/CIGS shown in Figure 10 after 75 h of aging in the in situ Raman cell ($45°C$, 82% RH, defocused laser illumination, three $(NH_4)_2SO_4$ drops) and corresponding Raman spectra.

map (Figure 10, Raman mapping acquisition at 5% laser power, and 2 s in StreamLineHR© Mode). The heterogeneity of the spatial distribution of species is evident. Its center is constituted of 303, 380, 809, and 891 cm^{-1} peaks attributed to Na_2MoO_4. It is surrounded by a product exhibiting peaks at 121, 305, 326, 425, 651, 766, 809, 826, 853, 897, 928, and 1067 cm^{-1}. Similar to Figure 8, the product is identified as a mix of peaks of Na_2MoO_4 (305, 809, and 897 cm^{-1}), carbonate (peaks 1070 cm^{-1}[150]), and possibly $Na_2Mo_2O_7$ (121, 766, 826, and 853, 928 cm^{-1}) and Ga_2O_3 (responsible for 326, 425, 651 cm^{-1}[154]). The EDS signal of this area (Na, C, and O) led to identify of the carbonate as sodium carbonate Na_2CO_3; the Raman signal of the ν_1 (A'$_1$) main peak is, however, less intense than in the in situ measurement. $Cu_{2-x}Se$ (peak at 259 cm^{-1}) is present mainly on the borders of the spot.

It is worth noticing the dynamics of the dark spots formation in the in situ Raman cell. The growth was very fast during the first 24 h, and during this period, the spots contained Na_2MoO_4. Later, the expansion was much slower, and in the places where carbonate species, the most probably Na_2CO_3, were detected, no simple molybdate Na_2MoO_4 but partly polymerized dimolybdate $Na_2Mo_2O_7$ was detected. Another interesting observation was that the front of $Cu_{2-x}Se$ expanded from the center of the dot with time, and the expansion of this species was quicker than that of Na_2MoO_4, suggesting that the initial transformation of CIGS is needed to degrade the underlying molybdenum layer. Interestingly, if in the beginning the Raman peaks of $Cu_{2-x}Se$ in the center of the spot increased compared with CIGS (spectra at 26 and 43 h in Figure 9), $Cu_{2-x}Se$ signal seems to disappear once Na_2MoO_4 was transformed into $Na_2Mo_2O_7$ and gallium oxide was detected (spectra at 43 and 69 h in Figure 9).

The proposed identification and spatial distribution of species on the basis of Raman spectroscopy were also confirmed by SEM observations and EDS analysis of the center of a dark spot formed on the CIGS surface after the end of the in situ experiment (Figure 11).

The EDS spectra of the crystals of corrosion products, visible on the surface after the experiment (Figure 11A), evidenced mainly Na, Mo, and O, confirming the presence of the most probably precipitated molybdates on the top surface. After rinsing (Figure 11B), the crystals are not visible and the EDS spectra do not show Mo signal, confirming that this molybdate is soluble. The EDS spectra of the underlying dark surface demonstrated the presence of high carbon signal. The latter is consistent with the detection of carbonate peaks in Raman spectra.

Figure 11C represents high resolution image of the CIGS morphology in the area, indicated in Figure 11B, which represents the interface between darker (degraded) area on which Mo-containing products were detected, and lighter (less degraded) zone. The porosity of CIGS is clearly higher in the left part of the image, corresponding to the dark zone formed under Mo corrosion products. This observation is consistent with the suggestion that CIGS degradation allows transport of Mo corrosion products from the buried Mo, presumably by diffusion.

4 | DISCUSSION: ROLE OF MO/CIGS INTERFACE FOR STABILITY OF EACH LAYER

4.1 | Importance of Mo for CIGS stability

The results shown in previous sections demonstrated strong differences in the stability of SLG/Mo/CIGS and SLG/CIGS samples. Additionally, molybdenum corrosion products were also detected on the top surface of CIGS layer in the SLG/Mo/CIGS surface. CIGS is still detected underneath the products (Figures 7 and 8) so the CIGS layer is still present but is more porous. It supports the importance of molybdenum in degradation mechanisms of CIGS and suggests possible diffusion of soluble molybdenum species through the CIGS layer from Mo/CIGS interface to the top of the CIGS. The migration of
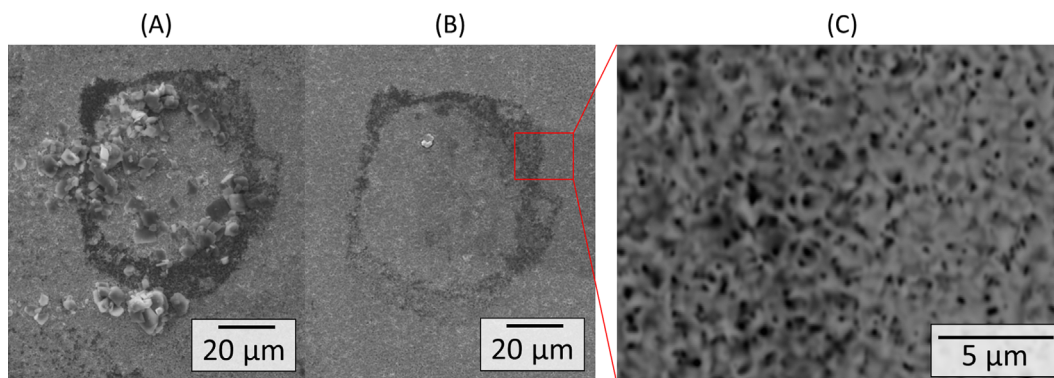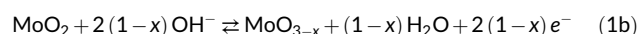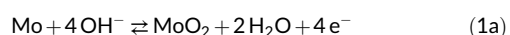
FIGURE 11   SE images of SLG/Mo/CIGS after 75 h aging in the in situ Raman cell (45°C, 82% RH, under laser illumination with $(NH_4)_2SO_4$ drops) before (A) and after (B) rinsing the sodium molybdate compound. (C) Backscattered electron (BSE) image of the interface between the dark spot and "intact" CIGS matrix shown by the red square in (B).

molybdenum is relevant not only for small assemblies but also for CIGS encapsulated modules. It was indeed reported that molybdenum-based compounds like oxides are detected on top of TCO layer, as a result of the delamination of EVA and migration of molybdenum from P3 scribe.[56]

The experiments also demonstrated that at studied degradation times soluble molybdenum species (Na_2MoO_4 and $Na_2Mo_2O_7$) can be detected only on the samples in which molybdenum was buried and therefore not directly exposed to the humid atmosphere (either encapsulated SLG/Mo/Al_2O_3 and SLG/Mo/CIGS/Al_2O_3 or SLG/Mo/CIGS, Figures 5 and 7–10). With pollutants like Na_2SO_4, corrosion is more advanced, so these molybdates were detected even for SLG/Mo (Figure 5). For the samples in which molybdenum was exposed directly to the atmospheres, only a mixture of the oxides was detected, strongly supporting the hypothesis of the importance of confined zone for the degradation mechanisms and formation of soluble molybdenum species. To understand this difference, the chemistry of both molybdenum and CIGS degradation on the open surface and in confined zone need to be detailed.

4.2 | Difference of molybdenum aging on open surface and in confined zone at Mo/CIGS interface

Atmospheric species like O_2 and H_2O could reach Mo/CIGS or Mo/Al_2O_3 interface by defects (cut edges, pores, or grain boundaries of CIGS or pits in the encapsulating Al_2O_3).[57] In accordance with thermodynamics,[55,58,59] metallic molybdenum is unstable in the presence of humidity and oxygen[58] and a layer of oxides forms on the surface thanks to anodic oxidation (Reaction 1). The exact nature of this layer depends on the aging conditions, and it is debated in the literature, but usually, it is a mixture of probably not well-defined oxides, with oxidations states of molybdenum between +IV and +VI, like MoO_2, MoO_3, Mo_8O_{23}, and Mo_4O_{11}.

$$Mo + 4OH^- \rightleftarrows MoO_2 + 2H_2O + 4e^- \quad (1a)$$

$$MoO_2 + 2(1-x)OH^- \rightleftarrows MoO_{3-x} + (1-x)H_2O + 2(1-x)e^- \quad (1b)$$

At the same time, cathodic oxygen reduction (Reaction 2) contributes to the increase of alkalinity in cathodic areas, thus advancing higher oxidation states of Mo (Reaction 1b).

$$O_2 + 2H_2O + 4e^- \rightleftarrows 4OH^- \quad (2)$$
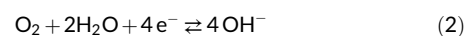
In the present work, MoO_2, MoO_3, and Mo_8O_{23} were indeed detected on SLG/Mo samples in which molybdenum in the tests was directly exposed to the humid atmosphere (Figures 4 and 5).

A particularity of corrosion in the confined zone is that because of the small volume of the electrolyte and limited spreading (washing) of species, their accumulation, and hence the pH increase, is much quicker than on the open surface. Also, oscillations in pH and in the quantity of corrosion products could be observed, related to the low quantity of water in the confined reaction volume, water consumption by oxygen reduction, and water regeneration after precipitation of the oxides.[60] As a result of rapidly achieved high alkalinity, the oxides are unstable in confined zone, which results in their immediate dissolution with formation of soluble molybdates anions (Reaction 3). The equations are written in the case of MoO_2 (Reaction 3.a) and MoO_3 (Reaction 3.b), but a reaction with a mixture of these can also occurs.

$$MoO_2 + 4OH^- \rightleftarrows MoO_4^{2-} + 2H_2O + 2e^- \quad (3a)$$

$$MoO_3 + 2OH^- \rightleftarrows MoO_4^{2-} + H_2O \quad (3b)$$
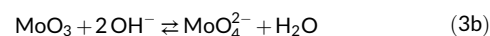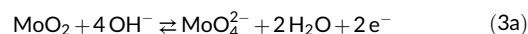
High solubility of molybdate anions explains their rapid diffusion with the electrolyte through the pores of CIGS to the top surface. Na^+ ions are known to accumulate at grain boundaries of CIGS, at CIGS/Mo interface, and even in the molybdenum layer.[61,62] In contact with the electrolyte containing MoO_4^{2-} anions, cations Na^+ can be leached by charge compensation. Moreover, the presence of Na^+ could be another factor increasing corrosion rate because sodium is

known as one of the most corrosive cations. For instance, on zinc and carbon steel, it was found to be the most aggressive among all the tested metallic cations.[63,64] The sodium content in the layers could hence be an important factor for stability, and probably, a compromise content needs to be defined to keep good performance but does not degrade stability of the Mo/CIGS interface. Drying of the electrolyte will lead to the precipitation of sodium molybdate on the surface (Reaction 4).

$$2\,Na^+ + MoO_4^{2-} \rightleftharpoons Na_2MoO_4 \qquad (4)$$

Na_2MoO_4 was indeed detected ex situ after several days of climatic chamber tests and/or in situ for all the samples in which molybdenum was buried (SLG/Mo/Al$_2$O$_3$, SLG/Mo/CIGS and SLG/Mo/CIGS/Al$_2$O$_3$). This species was also observed at advanced stages of corrosion of molybdenum in SLG/Mo systems after 1000 h of DH test at 85°C/85%[18] and after immersion in deionized water for 24 h at 50°C.[26] It was also described as a possibility in Lin et al.[19]

An important observation is that with the advancement of degradation or after long storage of degraded samples, most of Na_2MoO_4 condensed into di-molybdate $Na_2Mo_2O_7$ (Reaction 5):

$$2\,MoO_4^{2-} + 2\,H_3O^+ \rightleftharpoons Mo_2O_7^{2-} + 3\,H_2O \qquad (5)$$
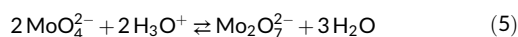
This transformation, confirmed also by the in situ experiment (Figure 9) and species distribution (Figure 10), requires some decrease of pH, which is also coherent with the stability diagrams.[55] Slight pH decrease and accumulation of soluble carbonates are indeed expected on the top surface thanks to a gradual dilution of the solution exposed to humid atmosphere and adsorption of atmospheric CO_2 (Reaction 6).

$$CO_2 + NaOH \rightarrow NaHCO_3 \qquad (6a)$$

$$CO_2 + 2\,NaOH \rightarrow Na_2CO_3 + H_2O \qquad (6b)$$
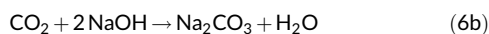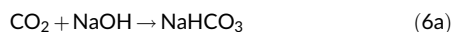
Indeed, soluble carbonates were detected in the in situ experiment in the same locations as polymolybdates.

## 4.3 | CIGS chemical evolution near Mo/CIGS interface

As discussed in Section 4.1, CIGS degradation was strongly enhanced by the presence of underlying Mo layer. In our mechanistic approach, we do not separate specifically MoSe$_2$ interlayer, even it is for sure present at the Mo/CIGS interface. Such a choice can be justified by the fact that, according to the recent work,[9] the role of MoSe$_2$ layer in relation with degradation processes is to form a barrier for the diffusion of oxygen and humidity to Mo, but its presence does not result in formation of different corrosion products. The latter allows us to suggest that the presence of MoSe$_2$ could slow the kinetics but does not change Mo and interface degradation mechanisms, and we

do not mention it in the figure for simplicity. We limit therefore the discussion to the effect of Mo layer reactivity on the stability of Mo/CIGS interface. The observed effect could be explained by the pH increase in the confined zone, discussed in the previous section, thanks to Mo corrosion and chemical reactions of CIGS with this alkalinized electrolyte (also containing other soluble ions) through porosity of CIGS layer. First of all, sodium leaching from grain boundaries is expected to be stronger in contact with the electrolyte containing anions, which also can contribute to the alkalinity increase. Previous works demonstrated that in sufficiently humid environment (RH 60%), Ga and In are first leached from CIGS forming the oxides (Ga$_2$O$_3$ and In$_2$O$_3$).[22] In the case of high alkalinity of the electrolyte, which is expected at the buried Mo/CIGS interface, and the elevated temperature of the test, similar to Al$_2$O$_3$, Ga oxides are expected to dissolve in the form of tetragallate anions [Ga (OH)$_4$]$^-$ (Reaction 7):

$$Ga_2O_3(solid) + 3H_2O + 2OH^- \rightleftharpoons 2\left[Ga(OH)_4\right]^- \qquad (7)$$
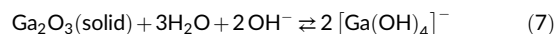
Dissolution of the oxide can further enhance Ga leaching from CIGS. In this work, we discuss the alkaline dissolution of Ga oxides because in the studied architecture, the CIGS close to the molybdenum interface was enriched by Ga and poor in In, as illustrated by GD-OES elemental depth profiles shown in the supporting information (Figure S3).

In contrast to Ga, Cu stays insoluble at high pH,[65] while Se^{2-} can be oxidized either to metallic Se^0 or even to soluble selenides anions SeO$_4^{2-}$.[66] Indeed, Se^0 is often found on the surface of CIGS by XPS.[67–69] In our work, gallium-containing corrosion products were indeed detected at advanced stages of degradation (Figure 9, spectrum at 69 h, Figure 10 spectrum 3). The detected peaks, however, correspond better to Ga$_2$O$_3$ and GaOOH[54] than to [Ga (OH)$_4$]$^{2-}$. Such a modification of the gallium-containing product can, however, be easily understood from the fact that [Ga (OH)$_4$]$^-$ will be unstable on the surface because of dilution during humid stage, temperature decreases at dry stage, and pH decrease by the incorporation of CO_2 from air (Reaction 6). The correlation observed between the detection of gallium oxides and the presence of Na$_2$CO$_3$ in the same area (Figure 9, spectrum at 43 h and Figure 10, spectrum 3) supports the idea of that CO_2 adsorption from air causes the decomposition of this soluble complex and formation of the gallium oxides (for instance by Reaction 8).

$$2\,Na\left[Ga(OH)_4\right] + CO_2 \rightarrow Na_2CO_3 + Ga_2O_3 + 4\,H_2O \qquad (8)$$
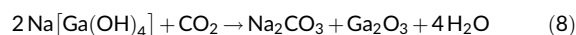
The mechanisms of the degradation of SLG/Mo and SLG/Mo/CIGS interface taking into account the formation of confined zone and the interplay between the layers are schematically summed up in Figure 12.

To sum up, gallium leaching from CIGS stimulated by pH increase could explain the enhanced formation of Cu$_{2-x}$Se phase detected by Raman in black dots. Moreover, the in situ experiment demonstrated that the increase of the Cu$_{2-x}$Se peak intensity correlated with the
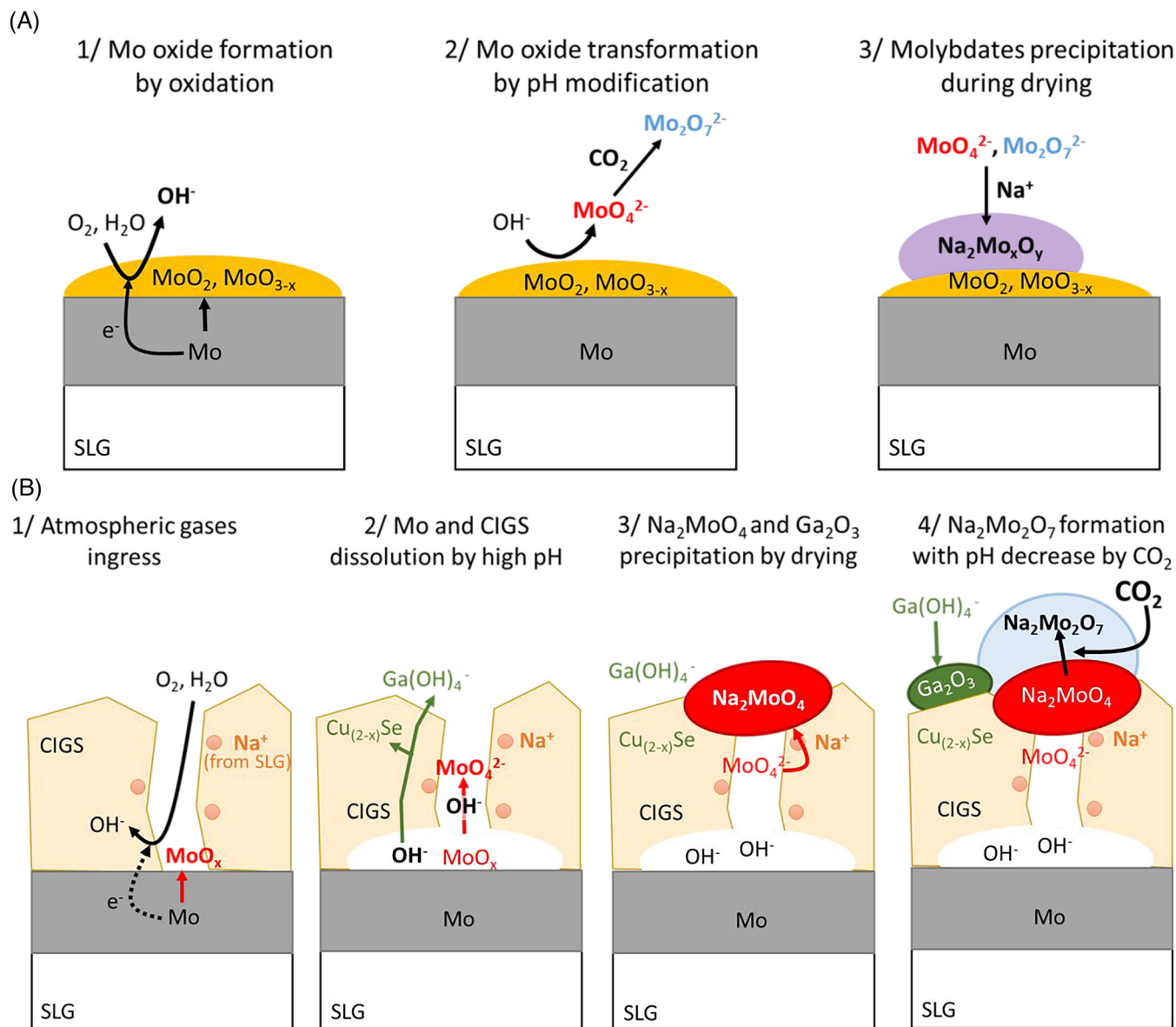
(A)

(B)

FIGURE 12   Hypothetical mechanisms of Na_2MoO_4 and $Na_2Mo_2O_7$ formation on (A) SLG/Mo and (B) SLG/Mo/CIGS.

detection of soluble Na_2MoO_4 (Figure 9, spectra at 26 and 43 h). Sodium (and potassium) migration during aging through the solar cell was already described in the literature.[15,20,26,70] Sodium is reported beneficial for cell performance[71] but detrimental for long-term stability, decreasing the fill factor and open circuit potential.[20,26,70] Sodium accumulates at the CIGS grain boundaries, forming shunt paths that degrade electrical properties of the cell.[8] Diffusion of anions such as molybdates through the CIGS layer is expected to increase Na^+ migration thus contributing to the accelerated degradation. Both sodium and gallium leaching could therefore decrease the optical properties of the layer. The transformation of CIGS also results in its porosity increase indeed demonstrated by SEM observation of the black dots after rinsing (Figure 11C), which accelerates the degradation of the underlying Mo.

5 | CONCLUSIONS

The outdoor stability of thin film materials relevant for CIGS solar cell was investigated using novel accelerated aging tests. Sputtered molybdenum back contact and co-evaporated CIGS absorber layer, deposited on soda lime glass or stacked together, were exposed to temperature and humidity cycles (25°C at 85% RH/80°C at 30% RH) with and without atmospheric pollutants (drops of NaCl, Na_2SO_4, and $(NH_4)_2SO_4$ representing coastal, rural, and agricultural atmospheres). Forecasting an increasing demand for flexible modules, the efficiency of inorganic thin film encapsulation was tested.

ALD-Al_2O_3 encapsulation layer efficiently protected the samples against temperature and humidity without pollutants, consistent with the conclusions from the DH test.[11] However, it failed to protect the

samples in the presence of the pollutants. The detailed effects of pollutants on the degradation mechanisms were not in the scope of this paper but could be relevant for further understanding of the effects of atmospheric chemistry on the stability of solar cells.

Unencapsulated molybdenum degraded forming multiple partly soluble molybdenum oxides, especially MoO_2, MoO_3, Mo_8O_{23}, detected using Raman spectroscopy. Additional products were also observed in the presence of pollutants, in particular Na_2MoO_4 and $Na_2Mo_2O_7$ mostly in confined environment for unencapsulated and encapsulated molybdenum.

In case of unencapsulated SLG/CIGS samples, Raman and XRD did not evidence any chemical modification during and after 2 weeks of aging. It was concluded that the layer is quite stable in time with regard to temperature, humidity, and pollutants.

SLG/Mo/CIGS samples after aging were much more degraded than SLG/CIGS. Visual observation evidenced the formation of dark spots. If the Raman spectrum of CIGS did not change much outside the spots, new products were detected inside the spot. Enhanced degradation of SIGS on Mo compared with its degradation on SLG was explained considering the solution chemistry modification near the Mo/CIGS interface because of corrosion of buried Mo layer through the porosity of CIGS. In particular, the formation of copper selenide $Cu_{2-x}Se$ and sodium molybdates is detected on the top surface of CIGS after short exposures in humid atmospheres using Raman and EDS. It is attributed to be promoted by the pH increase at Mo/CIGS interface because of cathodic reaction during Mo corrosion and following diffusion of soluble species. Alkalinity increase is also believed to enhance Ga leaching from the CIGS because of formation of soluble tetragallate complexes. The latter could reform Ga_2O_3 on the top surface of the CIGS when pH is decreased by dilution and CO_2 adsorption, as also observed by in situ Raman experiment. Similarly, the transformation of Na_2MoO_4 into $Na_2Mo_2O_7$ with advancement of degradation and during storage at low humidity can be explained by slight acidification of the surface which is expected by CO_2 adsorption.

In situ Raman characterization during aging confirmed that Na_2MoO_4 initially formed inside the dark spots and after a few hours diffused to larger distances and polymerized into $Na_2Mo_2O_7$ at the periphery. In situ detection of $Cu_{2-x}Se$ on the dark zone periphery was also coherent with the CIGS degradation which can be enhanced by pH increase in confined zone because of molybdenum corrosion. At the same time, the increased porosity of CIGS layer in the degraded zones, observed after the experiment by SEM, is expected to enhance further degradation of the underlying molybdenum layer as well as diffusion of soluble molybdates and gallates to the surface.

The observed strong effect of buried molybdenum on the stability of the top CIGS layer and the discussed degradation mechanisms highlights the importance of buried interfaces for stability evaluation of PV cells and necessity of understanding degradation mechanisms. Further work is, however, necessary to verify the impact of each interface in the complete stack as well as to test the effect of electrical current and illumination on the degradation mechanisms and degradation kinetics.

The methodology proposed in this work could be extended to access degradation mechanisms in other types of photovoltaic cells and to include variety of environments and exploitation conditions to monitor chemical evolution under illumination or *operando* considering the evolving chemistry in different applications (coastal environments for floating PV, agricultural environments for Agri-PV, etc).

DATA AVAILABILITY STATEMENT

ORCID

Adèle Debono https://orcid.org/0009-0000-0515-0102
Amelle Rebai https://orcid.org/0009-0006-4822-1349
Inger Odnevall https://orcid.org/0000-0003-2206-0082
Nathanaelle Schneider https://orcid.org/0000-0001-7749-2400
Jean-François Guillemoles https://orcid.org/0000-0003-0114-8624
Andreas Erbe https://orcid.org/0000-0002-7777-2258
Polina Volovitch https://orcid.org/0000-0001-5729-9830

REFERENCES

1. NREL. 'Best research cell efficiency chart'. Photovoltaic Research. [Online]. Available: https://www.nrel.gov/pv/assets/pdfs/best-research-cell-efficiencies-rev220630.pdf

2. Edoff M. 'State of the art and future prospects of thin film CIGS solar cells', presented at the state of the art and future prospects of thin film CIGS solar cells, Université du Luxembourg, 2023. [Online]. Available: https://wwwde.uni.lu/forschung/fstm/dphyms/news_events/physics_colloquium_state_of_the_art_and_future_prospects_of_thin_film_cigs_solar_cells_invited_speaker_prof_marika_edoff_from_uppsala_university

3. Mufti N, Amrillah T, Taufiq A, et al. Review of CIGS-based solar cells manufacturing by structural engineering. *Sol Energy*. 2020;207: 1146-1157. doi:10.1016/j.solener.2020.07.065

4. Feurer T, Reinhard P, Avancini E, et al. Progress in thin film CIGS photovoltaics—research and development, manufacturing, and applications: progress in thin film CIGS photovoltaics. *Prog Photovolt: Res Appl*. 2017;25(7):645-667. doi:10.1002/pip.2811

5. Ramanujam J, Bishop DM, Todorov TK, et al. Flexible CIGS, CdTe and a-Si:H based thin film solar cells: a review. *Prog Mater Sci*. 2020;110: 100619. doi:10.1016/j.pmatsci.2019.100619

6. International Electrotechnical Commission. International standard IEC 61215, crystalline silicon terrestrial photovoltaic (PV) modules—design qualification and type approval. Int Electrotech Comm IEC 61215–22016., 2016.

7. Zhang S, Maltseva A, Herting G, et al. Importance of atmospheric aerosol pollutants on the degradation of Al_2O_3 encapsulated Al-doped zinc oxide window layers in solar cells. *Prog Photovolt*. 2021; 30(5):552-566. doi:10.1002/pip.3527

8. Theelen M, Foster C, Steijvers H, Barreau N, Vroon Z, Zeman M. The impact of atmospheric species on the degradation of CIGS solar cells. *Sol Energy Mater Sol Cells*. 2015;141:49-56. doi:10.1016/j.solmat.2015.05.019

9. Theelen M, Broos RJP, Hovestad A. The influence of atmospheric species on the degradation of the $Mo/MoSe_2$ back contact in CIGS solar cells. *Mater Chem Phys*. 2022;279:125686. doi:10.1016/j.matchemphys.2021.125686

10. Reinhard P, Chirila A, Blosch P, et al. Review of progress toward 20% efficiency flexible CIGS solar cells and manufacturing issues of solar

modules. *IEEE J Photovolt*. 2013;3(1):572-580. doi:10.1109/JPHOTOV.2012.2226869

11. Zhang S-T, Guc M, Salomon O, et al. Effective module level encapsulation of CIGS solar cells with Al_2O_3 thin film grown by atomic layer deposition. *Sol Energy Mater Sol Cells*. 2021;222:110914. doi:10.1016/j.solmat.2020.110914

12. Theelen M, Daume F. Stability of Cu (In,Ga)Se_2 solar cells: a literature review. *Sol Energy*. 2016;133:586-627. doi:10.1016/j.solener.2016.04.010

13. Kempe MD, Terwilliger KM, Tarrant D. Stress induced degradation modes in CIGS mini-modules. In: *2008 33rd IEEE Photovolaic Specialists Conference*. IEEE; 2008:1-6. doi:10.1109/PVSC.2008.4922497

14. Feist R, Rozeveld S, Kern B, D'Archangel J, Yeung S, Bernius M. Further investigation of the lifetime-limiting failure mechanisms of CIGSS-based minimodules under environmental stress. In: *2009 34th IEEE Photovoltaic Specialists Conference (PVSC)*. IEEE; 2009:002359-002363. doi:10.1109/PVSC.2009.5411323

15. Theelen M, Tomassini M, Barreau N, et al. The impact of selenisation on damp heat degradation of the CIGS back contact molybdenum. In: *2012 IEEE 38th Photovoltaic Specialists Conference (PVSC) Part 2*. IEEE; 2012:1-6. doi:10.1109/PVSC-Vol2.2012.6656703

16. Heinemann MD, Ruske F, Greiner D, et al. Advantageous light management in Cu (In,Ga)Se_2 superstrate solar cells. *Sol Energy Mater Sol Cells*. 2016;150:76-81. doi:10.1016/j.solmat.2016.02.005

17. Karki S, Deitz JI, Rajan G, et al. Impact of water ingress on molybdenum thin films and its effect on Cu (In,Ga)Se_2 solar cells. *IEEE J Photovolt*. 2020;10(2):696-702. doi:10.1109/JPHOTOV.2019.2959947

18. Theelen M, Harel S, Verschuren M, et al. Influence of Mo/$MoSe_2$ microstructure on the damp heat stability of the Cu (In,Ga)Se_2 back contact molybdenum. *Thin Solid Films*. 2016;612:381-392. doi:10.1016/j.tsf.2016.06.028

19. Lin S, Liu W, Zhang Y, et al. Adjustment of alkali element incorporations in Cu (In,Ga)Se_2 thin films with wet chemistry Mo oxide as a hosting reservoir. *Sol Energy Mater Sol Cells*. 2018;174:16-24. doi:10.1016/j.solmat.2017.08.022

20. Theelen M, Hans V, Barreau N, Steijvers H, Vroon Z, Zeman M. The impact of alkali elements on the degradation of CIGS solar cells: degradation of CIGS solar cells. *Prog Photovolt: Res Appl*. 2015;23(5):537-545. doi:10.1002/pip.2610

21. Béchu S, Bouttemy M, Vigneron J, Lincot D, Guillemoles J, Etcheberry A. Evolution of Cu (In,Ga)Se_2 surfaces under water immersion monitored by X-ray photoelectron spectroscopy. *Surf Interface Anal*. 2020;52(12):975-979. doi:10.1002/sia.6896

22. Béchu S, Bouttemy M, Guillemoles J-F, Etcheberry A. The influence of relative humidity upon Cu (In,Ga)Se_2 thin-film surface chemistry: an X-ray photoelectron spectroscopy study. *Appl Surf Sci*. 2022;576:151898. doi:10.1016/j.apsusc.2021.151898

23. Nishinaga J, Kamikawa Y, Koida T, Shibata H, Niki S. Degradation mechanism of Cu (In,Ga)Se_2 solar cells induced by exposure to air. *Jpn J Appl Phys*. 2016;55(7):072301. doi:10.7567/JJAP.55.072301

24. Pern FJ, Egaas B, To B, et al. A study on the humidity susceptibility of thin-film CIGS absorber. In: *2009 34th IEEE Photovoltaic Specialists Conference (PVSC)*. IEEE; 2009:000287-000292. doi:10.1109/PVSC.2009.5411676

25. Britt JS, Kanto E, Lundberg S, Beck M. CIGS device stability on flexible substrates. In: *2006 IEEE 4th World Conference on Photovoltaic Energy Conference*. IEEE; 2006:352-355. doi:10.1109/WCPEC.2006.279462

26. Karki S, Paul P, Deitz JI, et al. Degradation mechanism in Cu (In,Ga)Se_2 material and solar cells due to moisture and heat treatment of the absorber layer. *IEEE J Photovolt*. 2019;9(4):1138-1143. doi:10.1109/JPHOTOV.2019.2912707

27. Klinkert T. Comprehension and optimisation of the co-evaporation deposition of Cu (In,Ga)Se_2 absorber layers for very high efficiency

thin film solar cells. *Doctoral thesis*. Université Pierre et Marie Curie - Paris VI. 2015.

28. Leygraf C, Graedel T. Atmospheric corrosion. In: *Electrochemical Society Series*. Second ed. Wiley; 2016.

29. Mysliu E, Lunder O, Erbe A. Role of aluminium hydrides in localised corrosion of aluminium revealed by operando Raman spectroscopy. *Phys Chem Chem Phys*. 2023;25(16):11845-11857. doi:10.1039/D3CP00522D

30. O'Brien FEM. The control of humidity by saturated salt solutions. *J Sci Instrum*. 1948;25(3):73-76. doi:10.1088/0950-7671/25/3/305

31. Paire M, Shams A, Lombez L, et al. Resistive and thermal scale effects for Cu (In,Ga)Se_2 polycrystalline thin film microcells under concentration. *Energ Environ Sci*. 2011;4(12):4972. doi:10.1039/c1ee01661j

32. Baltrusaitis J, Mendoza-Sanchez B, Fernandez V, et al. Generalized molybdenum oxide surface chemical state XPS determination via informed amorphous sample model. *Appl Surf Sci*. 2015;326:151-161. doi:10.1016/j.apsusc.2014.11.077

33. Camacho-Lopez S, Cano-Lara M, Camacho-Lopez M. Fast growth of multi-phase MoO_x synthesized by laser direct writing using femtosecond pulses. *Crystals*. 2020;10(7):629. doi:10.3390/cryst10070629

34. Navas I, Vinodkumar R, Lethy KJ, et al. Growth and characterization of molybdenum oxide nanorods by RF magnetron sputtering and subsequent annealing. *J Phys D: Appl Phys*. 2009;42(17):175305. doi:10.1088/0022-3727/42/17/175305

35. Camacho-López MA, Escobar-Alarcón L, Picquart M, Arroyo R, Córdoba G, Haro-Poniatowski E. Micro-Raman study of the m-MoO_2 to α-MoO_3 transformation induced by CW-laser irradiation. *Opt Mater*. 2011;33(3):480-484. doi:10.1016/j.optmat.2010.10.028

36. Seguin L, Figlarz M, Cavagnat R, Lassègues J-C. Infrared and Raman spectra of MoO_3 molybdenum trioxides and $MoO3 \cdot xH2O$ molybdenum trioxide hydrates. *Spectrochim Acta A Mol Biomol Spectrosc*. 1995;51(8):1323-1344. doi:10.1016/0584-8539(94)00247-9

37. Dieterle M, Mestl G. Raman spectroscopy of molybdenum oxides. *Phys Chem Chem Phys*. 2002;4(5):822-826. doi:10.1039/b107046k

38. Cuando-Espitia N, Redenius J, Mensink K, Camacho-López M, Camacho-López S, Aguilar G. Influence of oxygen pressure on the fs laser-induced oxidation of molybdenum thin films. *Opt Mater Express*. 2018;8(3):581. doi:10.1364/OME.8.000581

39. List A, Mitterer C, Mori G, Winkler J, Reinfried N, Knabl W. 'Oxidation of sputtered thin films of molybdenum alloys at ambient conditions', presented at the 17th Plansee Seminar, 2009.

40. Ben Mabrouk K, Kauffmann TH, Aroui H, Fontana MD. Raman study of cation effect on sulfate vibration modes in solid state and in aqueous solutions. *J Raman Spectrosc*. 2013;44(11):1603-1608. doi:10.1002/jrs.4374

41. Saraiva GD, Paraguassu W, Freire PTC, Maczka M, Filho JM. Temperature-dependent Raman scattering study of K_2MoO_4. *Vib Spectrosc*. 2012;58:87-94. doi:10.1016/j.vibspec.2011.11.015

42. Luz-Lima C, Saraiva GD, Filho AGS, Paraguassu W, Freire PTC, Mendes Filho J. Raman spectroscopy study of Na2MoO4·2H2O and Na2MoO4 under hydrostatic pressure. *J Raman Spectrosc*. 2009;41(5):576-581. doi:10.1002/jrs.2468

43. Saraiva GD, Paraguassu W, Maczka M, Freire PTC, de Sousa FF, Mendes Filho J. Temperature-dependent Raman scattering studies on $Na_2Mo_2O_7$ disodium dimolybdate: temperature-dependent Raman scattering from $Na_2Mo_2O_7$. *J Raman Spectrosc*. 2011;42(5):1114-1119. doi:10.1002/jrs.2836

44. Theelen M, Polman K, Tomassini M, et al. Influence of deposition pressure and selenisation on damp heat degradation of the Cu (In,Ga)Se_2 back contact molybdenum. *Surf Coat Technol*. 2014;252:157-167. doi:10.1016/j.surfcoat.2014.05.001

45. Witte W, Kniese R, Powalla M. Raman investigations of Cu (In,Ga)Se_2 thin films with various copper contents. *Thin Solid Films*. 2008;517(2):867-869. doi:10.1016/j.tsf.2008.07.011

46. Choi I-H. Raman spectroscopy of $CuIn_{1-x}Ga_xSe_2$ for in-situ monitoring of the composition ratio. *Thin Solid Films*. 2011;519(13):4390-4393. doi:10.1016/j.tsf.2011.02.058

47. Insignares-Cuello C. 'Raman scattering based strategies for assessment of advanced chalcopyrite photovoltaic technologies: Characterisation of electrodeposited Cu (In,Ga)(S,Se)$_2$ solar cells'. *Doctoral thesis*. Institut de Recerca en Energia de Catalunya (IREC). 2015.

48. Tsoulka P. 'Local inhomogeneities in polycrystalline wide band gap $CuIn_{1-x}Ga_xSe_2$ thin-films'. Université de Nantes. 2017.

49. Rincón C, Ramírez FJ. Lattice vibrations of $CuInSe_2$ and $CuGaSe_2$ by Raman microspectrometry. *J Appl Phys*. 1992;72(9):4321-4324. doi:10.1063/1.352195

50. Buzgar N, Ionu A, Apopei Ţ. 'The Raman study of certain carbonates'. Analele Ştiinţifice ale Universităţii "Al I Cuza" IAŞI, seria Geologie. 2009;2:97–112.

51. Fortes AD, Wood IG, Alfè D, Hernández ER, Gutmann MJ, Sparkes HA. Structure, hydrogen bonding and thermal expansion of ammonium carbonate monohydrate. *Acta Crystallogr B Struct Sci Cryst Eng Mater*. 2014;70(6):948-962. doi:10.1107/S205252061402126X

52. Ma Y, Yan W, Sun Q, Liu X. Raman and infrared spectroscopic quantification of the carbonate concentration in K_2CO_3 aqueous solutions with water as an internal standard. *Geosci Front*. 2021;12(2):1018-1030. doi:10.1016/j.gsf.2020.03.002

53. Hunnius W-D. A polymeric ammoniumdimolybdate from aqueous solution. *Z Naturforsch B*. 1974;29(9-10):599-602. doi:10.1515/znb-1974-9-1005

54. Zhao Y, Frost RL. Raman spectroscopy and characterisation of a-gallium oxyhydroxide and b-gallium oxide nanorods. *J Raman Spectrosc*. 2008;39(10):1494-1501. doi:10.1002/jrs.2028

55. Nikolaychuk PA, Tyurin AG. The revised Pourbaix diagram for molybdenum. *Butlerov Commun*. 2011;24(2):101-105. doi:10.13140/2.1.2853.0883

56. Villa S, Aninat R, Yilmaz P, et al. Insights into the moisture-induced degradation mechanisms on field-deployed CIGS modules. *Prog Photovolt Res Appl*. 2023;31(8):1-16. doi:10.1002/pip.3689

57. Theelen M, Boumans T, Stegeman F, et al. Physical and chemical degradation behavior of sputtered aluminum doped zinc oxide layers for Cu (In,Ga)Se$_2$ solar cells. *Thin Solid Films*. 2014;550:530-540. doi:10.1016/j.tsf.2013.10.149

58. Lyon SB. Corrosion of molybdenum and its alloys. In: *Shreir's Corrosion*. Elsevier; 2010:2157-2167. doi:10.1016/B978-044452787-5.00106-2

59. Shkirskiy V, Keil P, Hintze-Bruening H, et al. MoO_4^{2-} as a soluble inhibitor for Zn in neutral and alkaline solutions. *Corros Sci*. 2015;99:31-41. doi:10.1016/j.corsci.2015.05.005

60. Iqbal D, Sarfraz A, Stratmann M, Erbe A. Solvent-starved conditions in confinement cause chemical oscillations excited by passage of a cathodic delamination front. *Chem Commun*. 2015;51(89):16041-16044. doi:10.1039/C5CC06468F

61. Braunger D, Hariskos D, Bilger G, Rau U, Schock HW. Influence of sodium on the growth of polycrystalline Cu (In,Ga)Se$_2$ thin films. *Thin Solid Films*. 2000;361–362:161-166. doi:10.1016/S0040-6090(99)00777-4

62. Yoon J-H, Seong T-Y, Jeong J. Effect of a Mo back contact on Na diffusion in CIGS thin film solar cells: effect of a Mo back contact on Na diffusion. *Prog Photovolt: Res Appl*. 2013;21(1):58-63. doi:10.1002/pip.2193

63. Lindström R, Svensson J-E, Johansson LG. The influence of salt deposits on the atmospheric corrosion of zinc. The important role of the sodium ion. *J Electrochem Soc*. 2002;149(2):B57. doi:10.1149/1.1432670

64. Prosek T, Thierry D, Taxén C, Maixner J. Effect of cations on corrosion of zinc and carbon steel covered with chloride deposits under atmospheric conditions. *Corros Sci*. 2007;49(6):2676-2693. doi:10.1016/j.corsci.2006.11.004

65. Celante VG, Freitas MBJG. Electrodeposition of copper from spent Li-ion batteries by electrochemical quartz crystal microbalance and impedance spectroscopy techniques. *J Appl Electrochem*. 2010;40(2):233-239. doi:10.1007/s10800-009-9996-x

66. Ralston NVC, Unrine J, Wallschläger D. 'Biogeochemistry and analysis of selenium and its species'. North American Metals Council. 2008.

67. Ramdani O, Chassaing E, Canava B, et al. Electrochemical cementation phenomena on polycrystalline molybdenum thin films from Cu (II)–In (III)–Se (IV) acidic solutions. *J Electrochem Soc*. 2007;154(8):383-393. doi:10.1149/1.2740041

68. Loubat A, Béchu S, Bouttemy M, et al. Cu depletion on Cu (In,Ga)Se$_2$ surfaces investigated by chemical engineering: an x-ray photoelectron spectroscopy approach. *J Vac Sci Technol A*. 2019;37(4):041201. doi:10.1116/1.5097353

69. Canava B, Vigneron J, Etcheberry A, Guillemoles JF, Lincot D. High resolution XPS studies of Se chemistry of a Cu (In, Ga)Se$_2$ surface. *Appl Surf Sci*. 2002;202(1–2):8-14. doi:10.1016/S0169-4332(02)00186-1

70. Daume F, Puttnins S, Scheit C, et al. Damp heat treatment of Cu (In,Ga)Se$_2$ solar cells with different sodium content. *Materials*. 2013;6(12):5478-5489. doi:10.3390/ma6125478

71. Rau U, Schock HW. Electronic properties of Cu (In,Ga)Se$_2$ heterojunction solar cells-recent achievements, current understanding, and future challenges. *Appl Phys A: Mater Sci Process*. 1999;69(2):131-147. doi:10.1007/s003390050984

SUPPORTING INFORMATION

Additional supporting information can be found online in the Supporting Information section at the end of this article.